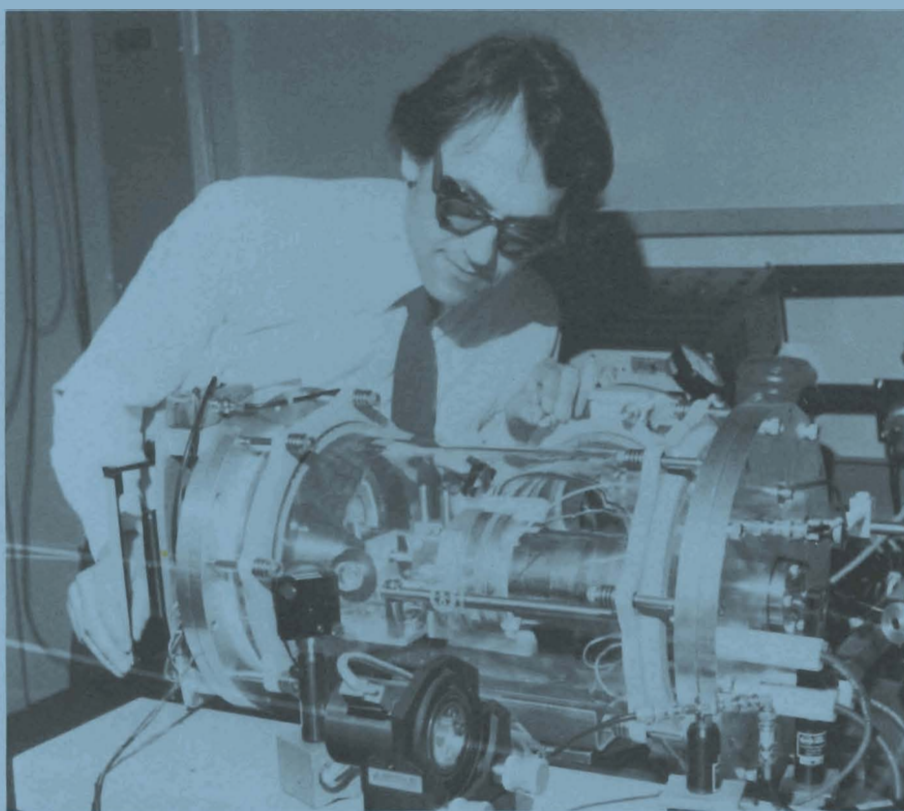


LLE Review

Quarterly Report



October - December 1982

Laboratory for Laser Energetics
College of Engineering and Applied Science
University of Rochester
250 East River Road
Rochester, New York 14623



LLE Review

Quarterly Report

Editor: R. S. Craxton
(716-275-5467)

October-December 1982

Laboratory for Laser Energetics
College of Engineering and Applied Science
University of Rochester
250 East River Road
Rochester, New York 14623



This report was prepared as an account of work conducted by the Laboratory for Laser Energetics and sponsored by Empire State Electric Energy Research Corporation, General Electric Company, New York State Energy Research and Development Authority, Northeast Utilities, The Standard Oil Co. (OHIO), University of Rochester, and various United States Government agencies.

Neither the above named sponsors, nor any of their employees, makes any warranty, express or implied, or assumes any legal usefulness of any information, apparatus, product, or process disclosed, or represents that its use would not infringe privately owned rights.

Reference herein to any specific commercial product, process, or service by trade name, mark, manufacturer, or otherwise, does not necessarily constitute or imply its endorsement, recommendation, or favoring by the United States Government or any agency thereof or any other sponsor.

Results reported in the LLE Review should not be taken as necessarily final results as they represent ongoing research. The views and opinions of authors expressed herein do not necessarily state or reflect those of any of the above sponsoring entities.

IN BRIEF

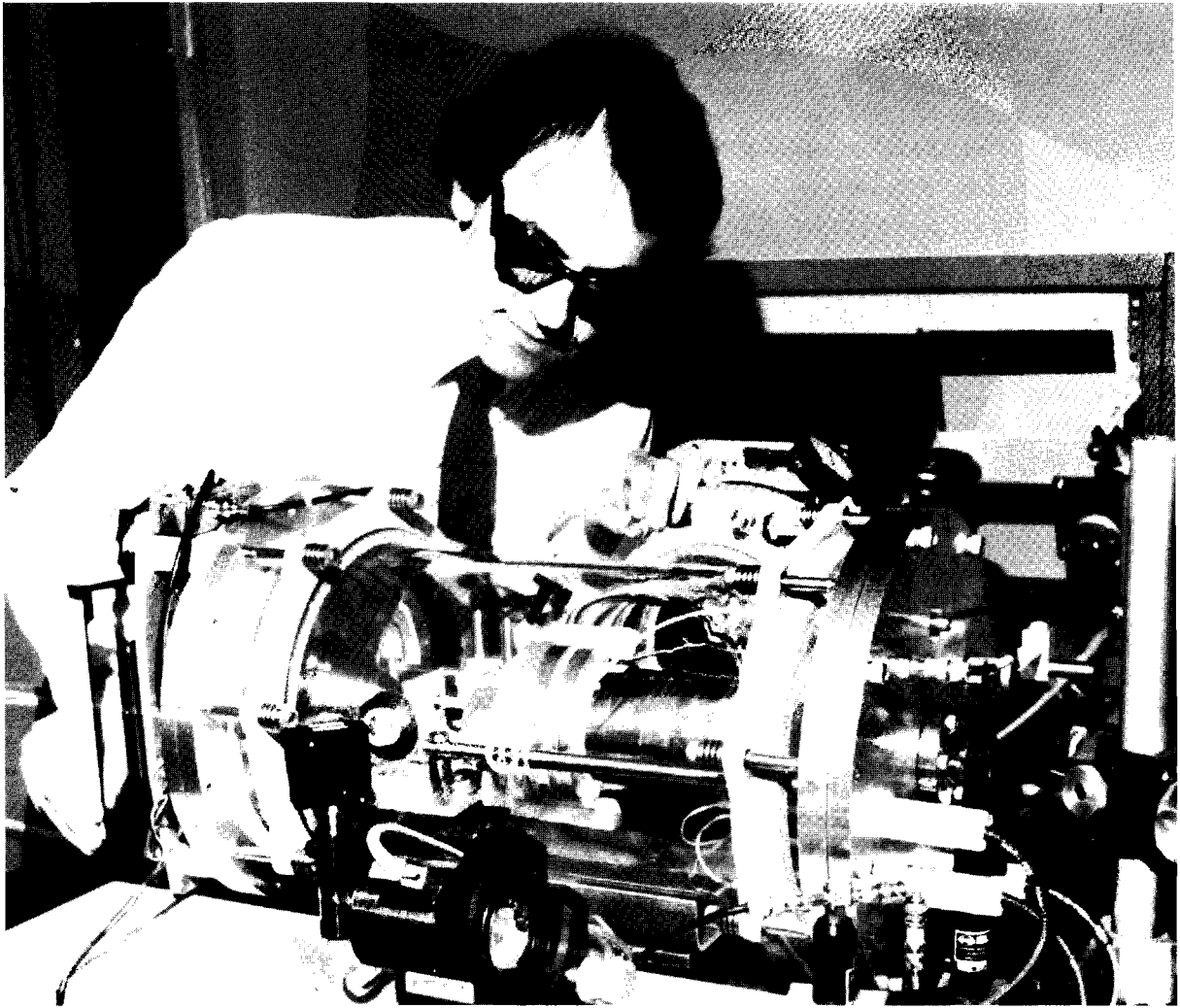
This edition of the LLE Review contains articles on target interaction experiments on OMEGA and GDL, characterization of symmetry on OMEGA, frequency-conversion technology, advances in target characterization and picosecond research, and NLUF experiments performed on OMEGA during the first quarter of fiscal year 1983 (October-December 1982). The following are some of the highlights of the work described in this issue:

- A theoretical analysis of illumination uniformity on spherical targets has been developed, using a spherical-harmonic decomposition of the energy deposition pattern of overlapping beams. Estimates show that uniformity levels of order 1% should be attainable.
- An extensive series of thermal-transport experiments at $1.05\ \mu\text{m}$ on OMEGA is reported. Transport in spherical geometry is found to differ from transport under comparable single-beam target irradiation conditions. The temperature profile in spherical geometry has been found to drop gradually rather than steeply into the target.
- Spherical targets on OMEGA have been photographed in their harmonic emissions at $2\omega_0$, $3\omega_0/2$, and $5\omega_0/2$. These emissions provide important information about instability phenomena occurring in the underdense region. Emissions of $2\omega_0$ and $5\omega_0/2$ from the quarter-critical region are reported for the first time.

- Measurements of the continuum x-ray spectra produced by IR- and UV-generated laser plasmas on GDL are reported. A "hard" component, originating from fast electrons produced by resonance absorption, is observed only for 1.05- μm radiation. A "super-hard" component, containing less than 0.1% of the incident laser energy, is seen at both wavelengths.
- A single, "monolithic", frequency-conversion cell has been designed, and will be used for the conversion of the first six beams of OMEGA to the UV. A prototype, containing a new index-matching fluid (Koolase™), has been successfully tested on GDL.
- An improved interferometric technique for the characterization of nonconcentricity in transparent inertial-fusion targets has been developed.
- An improvement in an LLE-developed system for time-resolving short electrical signals has led to the generation and measurement of a step-function electrical signal with a rise time of 850 fs.
- Shifts and widths of hydrogenic ion lines emitted by the dense plasmas generated on OMEGA have been observed in an NLUF experiment.

CONTENTS

	<i>Page</i>
IN BRIEF	iii
CONTENTS	v
Section 1 LASER SYSTEM REPORT	1
1.A GDL Facility Report	1
1.B OMEGA Facility Report	2
Section 2 PROGRESS IN LASER FUSION	5
2.A Characterization of Irradiation Uniformity on Spherical Targets	5
2.B Thermal Transport Measurements on OMEGA	12
2.C High-Resolution Harmonic Photography on OMEGA	18
2.D Continuum X-Ray Spectra from UV- and IR-Laser-Produced Plasmas	23
Section 3 TECHNOLOGICAL DEVELOPMENTS	30
3.A Monolithic Cell for Frequency Conversion	30
3.B Rotational-Shearing Interferometry for Improved Target Characterization	37
Section 4 BRIEF UPDATES	44
4.A Progress Toward Terahertz Electronics	44
Section 5 NATIONAL LASER USERS FACILITY NEWS	46
PUBLICATIONS AND CONFERENCE PRESENTATIONS	51



Gerard Mourou, senior scientist and leader of the Picosecond Group, making final adjustments to an apparatus in which picosecond electrical pulses are generated as replicas of picosecond optical pulses.

Section 1

LASER SYSTEM REPORT

1.A GDL Facility Report

GDL operations continued through this quarter virtually uninterrupted by any major failure. Shots were taken to support various interaction experiments, including Stimulated Raman and Stimulated Brillouin Scattering. Various diagnostics were tested before subsequent installation on OMEGA for the coronal-physics campaign. The NLUF was supported during two different periods for a combined Yale/UCLA experiment. Several x-ray-diffraction experiments, including biological-stimulus experiments, were conducted. Damage testing continued, although at a substantially diminished rate from the previous quarter. The quarter ended with a series of shots into the BETA tank in support of a transport experiment.

A total of 526 shots was delivered by the facility during the period October 1 to December 31, 1982. The shot distribution was as follows:

3ω Target Experiments	247	(47%)
Damage Test Facility	79	(15%)
X-Ray Chamber	80	(15%)
Miscellaneous (checkout, centering, calorimetry)	<u>120</u>	<u>(23%)</u>
TOTAL	526	(100%)

1.B OMEGA Facility Report

OMEGA activities during this quarter have consisted of (1) concluding the transport and uniformity experimental campaigns, (2) continuing support of the beam-balance program, (3) testing oscillator configurations for the upcoming x-ray-laser program, and (4) diagnostic checkouts for the coronal-physics campaign. Firing of the laser in support of the experimental campaigns continued through October, and the complete system was shut down in November for maintenance and various system upgrades. The system was reactivated in December for preliminary coronal-physics tests. With the exception of some brief testing of the oscillator in November, the system remained configured for long-pulse operation (1 ns).

The distribution of OMEGA system shots during the period October 1 to December 31, 1982 was as follows:

Target Shots	105	(36%)
Driver Alignment and Testing	84	(28%)
Beamline Checkout and Calibration	72	(24%)
Software Test and Timing	34	(12%)
TOTAL	295	(100%)

During the October experimental campaign, beam balance remained in the 6 to 8% vicinity, with repeated excursions below 5% and a worst case of 13%. Energy has consistently been within 10% of the shot specification. Not a single day of shooting was lost during this campaign, a tribute to the reliability of all components of the system. Beam profiles were observed to degrade somewhat, due to optical damage in the "A" splitter area (scheduled for replacement in January) and a creeping misalignment in the driver-line optics.

In the experimental area there was little new activity in October due to limited diagnostic demand. Transport experiments and uniformity experiments required only x-ray photographic diagnostics and neutronics, and thus no new instruments were activated. Excellent results were obtained in a time-resolved transport experiment using an x-ray streak camera borrowed from NRC, and an XUV spectrometer was successfully used on an NLUF experiment in conjunction with the Naval Research Laboratory.

While the system was shut down, several improvements were made to various subsystems. An exhaustive effort to realign the driver line has resulted in an improved beam profile both out of the driver and at the far field, or equivalent target plane. Figure 1 shows a photograph of the driver-line output, digitized and presented as a topographical plot, as well as an azimuthally averaged radial plot, showing a pronounced lack of spatial irregularities and an excellent beam profile. Figure 2 is the same representation of a beam in the equivalent target plane, at approximately 100 J.

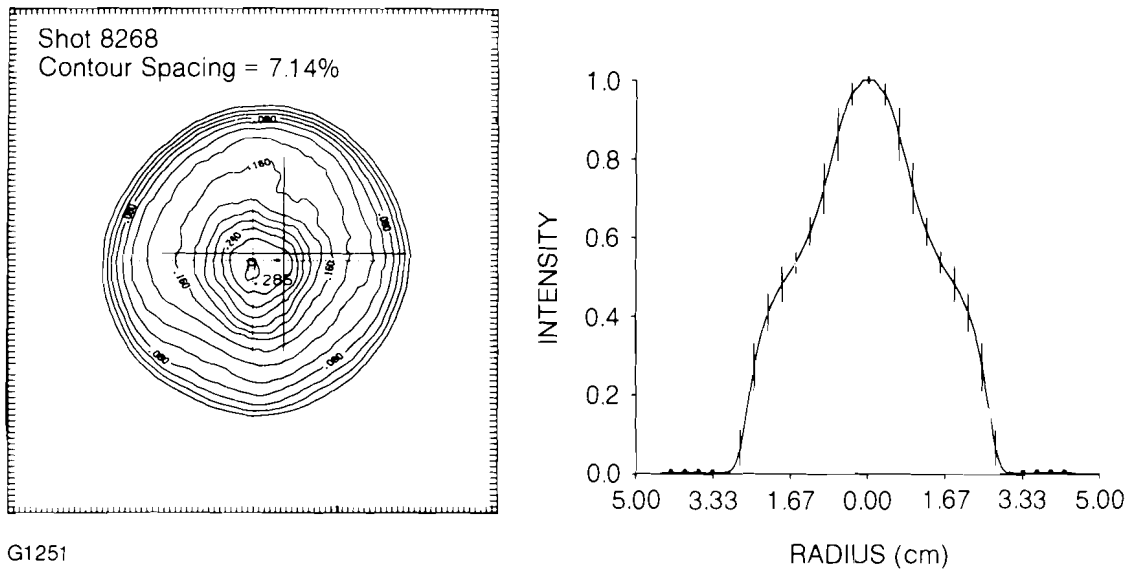


Fig. 1
Contour plot of the driver-line output (left)
and an azimuthally averaged radial profile
(right).

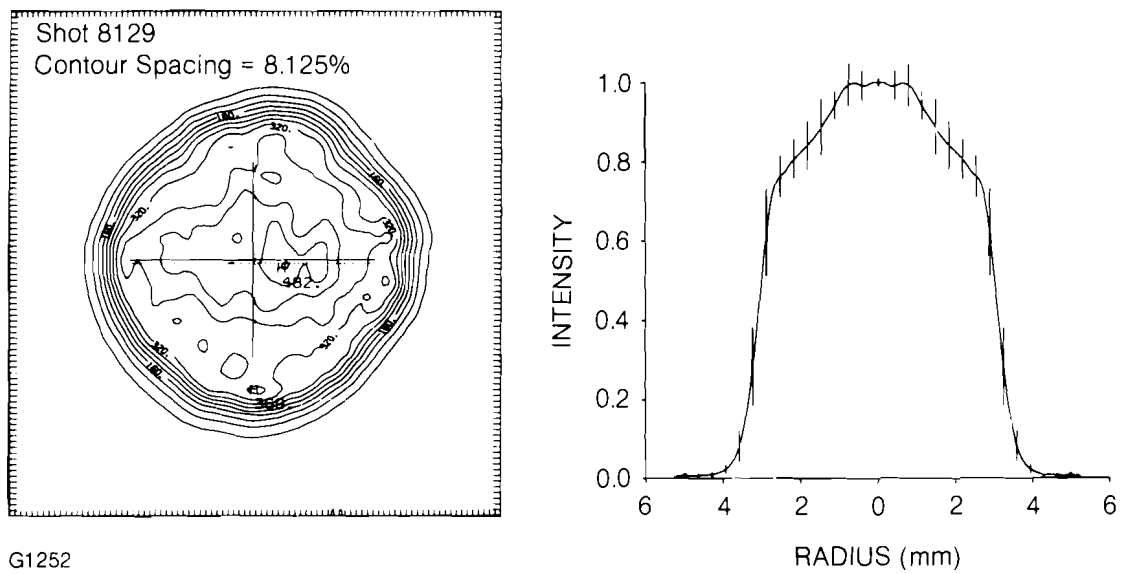


Fig. 2
Contour plot of a typical far-field beam
distribution (left) and an azimuthally aver-
aged radial profile (right).

The three-meter oscillator cavity underwent a brief configuration change, in an attempt to characterize its operation at a pulse width of approximately 50 ps in anticipation of the x-ray-laser program. The test resulted in quasi-stable operation at around 30 ps. The cavity configuration demonstrated about 75% stability. Due to a laser requirement for a beam-balance test the short-pulse tests were terminated, after lending support to the notion that stable 50-ps operation will be achieved when the proper etalon is installed.

Other improvements implemented during the shutdown period include a new (ISC) display in the power-conditioning system; this provides substantially more status information and control, and improves system reliability since backup hardware will now be available in-house. Work has progressed on the automated beam-timing system. Modifications were completed on two operations computer systems, *CER* and *MOMUS*, providing 22-bit capability and substantially more memory. The upgrade to *CER* will provide for the ongoing installation of the main diagnostic control task (*OPS*) and allow more memory for diagnostic acquisition and reduction tasks. With *OPS* installed in *CER*, the laser-diagnostic computer system (*AETHER*) will have more memory available for anticipated laser diagnostics. The *MOMUS* upgrade will provide a means for data archival, as well as a user setup for off-line software development, giving programmers the advantage of using real shot data for program evaluation.

As the laser system was reactivated, a 34-shot campaign aimed at calorimeter calibration was conducted. A single beam was split with calibrated beamsplitters into eight 8-inch calorimeters, whose positions were interchanged from shot to shot. The aim of the test was to eliminate beam-to-beam variation seen in the calorimeters in previous tests. The results of this successful campaign will be reported at a later date.

In the experimental area, the shutdown provided time to support the *CER* upgrade. In addition, film-advance controllers for x-ray diagnostics were modified to ensure more reliable operation and ease in monitoring return signals. Several diagnostics were adapted for OMEGA use, and activated as part of the coronal-physics campaign. These were: (1) an x-ray continuum spectrometer, (2) x-ray photomultiplier tubes, (3) $\omega_0/2$, $3\omega_0/2$, and $2\omega_0$ spectrometers, and (4) visible-harmonic-light diagnostics.

All systems were activated in December for a number of shots aimed at checking out and calibrating the diagnostic devices required for the coronal-physics campaign; a limited number of target shots was also provided for the Naval Research Laboratory NLUF experiment.

Section 2

PROGRESS IN LASER FUSION

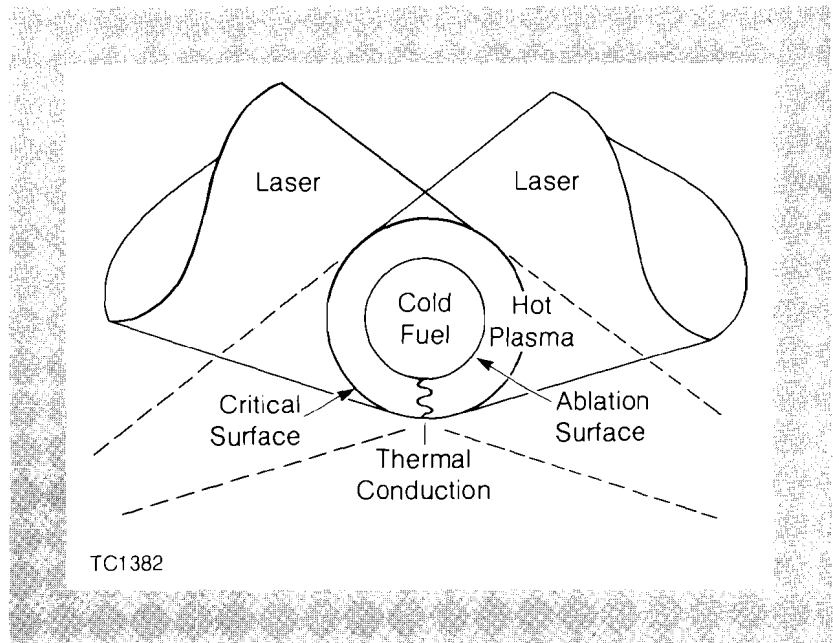
2.A Characterization of Irradiation Uniformity on Spherical Targets

To achieve high energy production by laser fusion, deuterium-tritium fuel must be compressed to ~ 1000 times its liquid density, and simultaneously heated above the ignition temperature (~ 5 keV) needed to sustain a thermonuclear burn.¹ The fuel is compressed and heated by depositing energy on the surface of a fuel-containing spherical target, causing surface material to be ablated, and driving the remainder of the target inward like a spherical rocket to implosion velocities greater than 10^7 cm/sec. For the method to be successful, a high degree of spherical convergence is required, placing severe constraints on the uniformity of energy deposition on the target surface. The level of nonuniformity in deposition that can be tolerated depends on the details of individual target designs; typically, an rms variation (σ_{rms}) of less than a few percent is required.²

Processes involved in direct laser drive are illustrated in Fig. 3. Shown schematically are two overlapping beams at tangential focus, each beam irradiating approximately half the target surface. The calculations below use examples with 24 and 32 such beams. Not shown in the figure, but included in our calculations, is the refraction of laser rays as they pass through the plasma atmosphere surrounding the target. After energy is deposited (which generally occurs close to the critical density), some of the nonuniformities in temperature are smoothed by thermal conduction^{3,4} as heat is transported inward to the ablation surface where the implosion is driven. The shorter-wavelength nonuniformities are more easily smoothed due to the prox-

Fig. 3

A high degree of irradiation uniformity can be achieved by overlapping laser beams. The laser light is refracted in the plasma atmosphere surrounding the target, with the majority of energy deposited near the critical density. Heat is then transported inward to the ablation surface where the implosion is driven. Some smoothing of nonuniformities in energy deposition can occur over the distance of heat transport.



imity of the hotter and colder regions. Thus, in examining the uniformity of energy deposition, we place considerable emphasis on calculating the spatial wavelengths of nonuniformities in addition to their magnitudes. This leads us to consider a spherical-harmonic decomposition of the laser-irradiation nonuniformity.

The uniformity of energy deposition in the target is calculated by tracing laser rays through the plasma atmosphere according to geometrical optics, and depositing energy along each ray trajectory by inverse bremsstrahlung. The calculation is greatly simplified by using beams with identical, azimuthally symmetric intensity profiles and perfectly spherical targets. Then the deposition pattern for only one beam need be calculated, and results for the other beams are obtained by rotation. To analyze the spatial variations of nonuniformities, the energy-deposition pattern is decomposed into spherical harmonics. The nonuniformity wavelength λ in each spherical-harmonic mode is related to the mode number ℓ approximately by:

$$\lambda = 2\pi R/\ell,$$

where R is the target radius. Thus $\ell=6$ corresponds to $\lambda \approx R$.

A useful measure of the illumination nonuniformity is the rms deviation defined as

$$\sigma_{\text{rms}} = \left\{ \frac{1}{4\pi} \int |E(\hat{r}) - \langle E \rangle|^2 dS \right\}^{1/2} / \langle E \rangle, \quad (1)$$

where $\langle E \rangle = \int E(\hat{r}) dS / 4\pi$, $E(\hat{r})$ is the total laser energy (summed over all beams) deposited between critical and 0.4 times critical density at an angular position determined by the unit vector \hat{r} , and dS is a surface element at \hat{r} . The energy-deposition pattern $E(\hat{r})$ is decomposed into Legendre polynomials and written as the sum of contributions from

the individual beams (with index k):

$$E(\hat{r}) = \sum_{\ell} \frac{2\ell+1}{2} E_{\ell} \sum_k W_k P_{\ell}(\hat{r} \cdot \hat{\Omega}_k). \quad (2)$$

Here all beams are assumed to have the same azimuthally symmetric profiles around their beam axes $\hat{\Omega}_k$, but the possibility of different energies, W_k , is allowed. The product $\hat{r} \cdot \hat{\Omega}_k$ is the cosine of the angle between a beam axis and an arbitrary unit vector \hat{r} (see Fig. 4).

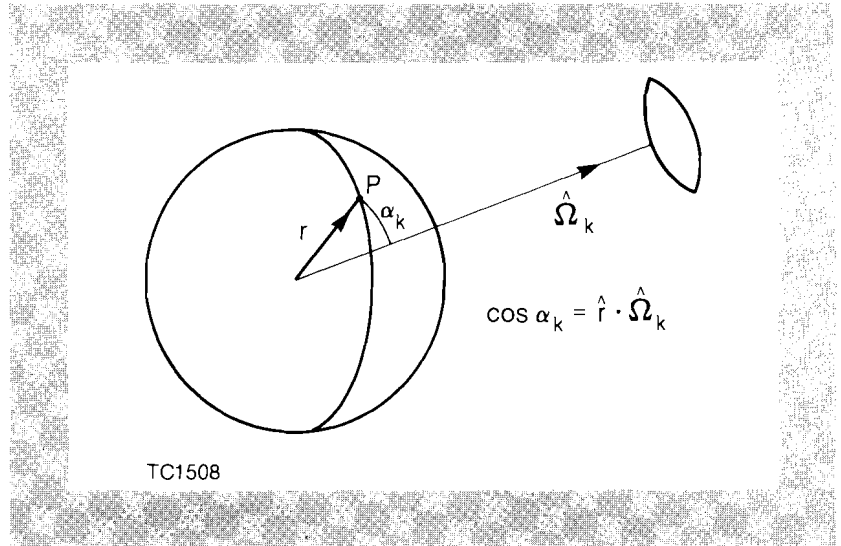


Fig. 4

The energy deposited at a point P is calculated by summing over a number of beams with identical azimuthally symmetric profiles. The contribution from beam k depends only on the angle α_k between \hat{r} and the beam axis and on the distance r from the target center.

Substituting Eq. (2) into Eq. (1) and using the orthogonality property of Legendre polynomials, σ_{rms} can be written explicitly in terms of the contribution from each ℓ -mode:

$$\sigma_{\text{rms}} = \left\{ \sum_{\ell \neq 0} \sigma_{\ell}^2 \right\}^{1/2} \quad (3)$$

where σ_{ℓ} is⁵:

$$\sigma_{\ell} = |E_{\ell}/E_0| \left\{ (2\ell+1) \sum_{k, k'} P_{\ell}(\hat{\Omega}_k \cdot \hat{\Omega}_{k'}) W_k W_{k'} / W_T^2 \right\}^{1/2}, \quad (4)$$

and where W_T is the total energy in the beams: $W_T = \sum W_k$.

Another measure of nonuniformity is the peak-to-valley variation $\Delta E/E$. We use σ_{rms} here because it can be expressed analytically [Eq. (4)], and the different factors can be examined directly. In contrast, the peak-to-valley variation requires a computer search over the target surface to find the extreme values of E. Typically, $\Delta E/E$ was found to be 3 to 5 times larger than σ_{rms} for the different cases examined.

The quantity σ_{ℓ} [Eq. (4)], characterizing the contribution of each mode to the overall nonuniformity, is factored into two terms:

- 1) The first term, $|E_{\ell}/E_0|$, is the energy-deposition pattern from a single beam which is determined by the focal position, intensity profile across the beam, lens f-number, and the density and

temperature profiles in the target plasma.

- 2) The second factor contains all the geometrical information about the laser system related to the number and orientation of the beams, and the energy balance between beams.

Clearly, the nonuniformity in a mode will vanish if conditions are found such that either factor is zero.

Two general results may be obtained just from the geometrical symmetry of the laser system, independent of the details about beam overlap or the laser absorption process. One is that all odd-order values of σ_ℓ vanish for any system with opposing beams and perfect beam energy balance. This occurs because the irradiation patterns on both sides of any great circle around the target are the same. A second result is that if N beams are uniformly distributed, then the lowest dominant mode of nonuniformity is given approximately by:

$$\ell = \pi \sqrt{N}/2.$$

As an example, for the 32-beam system discussed below, the geometrical term essentially eliminates all modes below $\ell = 10$. The magnitudes of the modes 10 and above are affected by the single-beam factor, which can even be "tuned" to eliminate some of these modes by means of profile shaping and focus adjustment.

Uniformity Results

The effects of specific laser-target conditions are illustrated here using as examples: (1) the 24-beam OMEGA laser system, and (2) a 32-beam system ("truncated" icosahedron) comprised of beams whose axes penetrate the centers of the 20 faces and the 12 vertices of an icosahedron. The first illustrates the uniformity potentially available with a currently operating laser system. The second illustrates that high uniformity can be attained even with high-f-number optics as required for future fusion reactors. (A high f-number is required to keep the final optical elements as far from the target explosion as possible.⁶)

In our calculations, we have considered the following variables: (1) radial laser intensity profile, (2) focus, (3) beam number and configuration, (4) plasma density profile in the target, (5) energy balance between beams, and (6) beam-target alignment. Beam imbalance and laser-target misalignment are found⁶ to be the main contributors to the long-wavelength modes ($\ell \leq 4$), and the remaining variables are responsible for shorter-wavelength nonuniformities. We calculate σ_{rms} from Eqs. (3) and (4) using the first 40 modes.

All of the examples given here use a 500- μm -radius target. The plasma atmosphere is at a temperature of 3 keV, with a distance of 10 μm between the critical and one-third-critical density radii and an exponential density profile with a scale length of 50 μm beyond. Such double-scale-length profiles are obtained in computer simulations of high-intensity laser irradiation with flux-limited heat flow.⁷ All the energy deposited in the short-scale-length (10- μm) region should contribute about equally to the implosion as this region covers a range of

just a few electron mean free paths. However, the energy deposited beyond one-third critical density can be at a relatively long distance from the ablation surface and should be less effective in driving the target. Since we are interested in drive uniformity, this distant energy deposition is not included here in the calculation of σ_{rms} in order to obtain a conservative estimate. This energy represents about 15% of the total and is relatively uniformly distributed; when it is included, σ_{rms} is reduced by a few percent.

The rms variation in energy deposition for the 24-beam system is shown in Fig. 5 as a function of focus, for three different radial beam

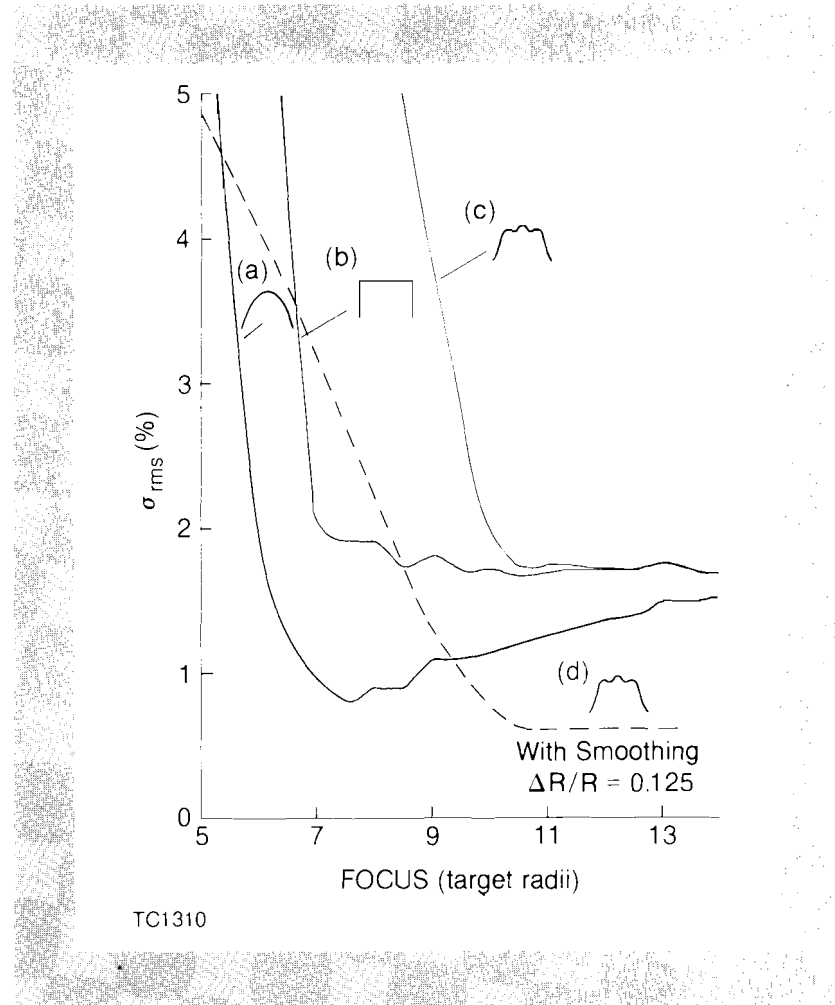


Fig. 5 Intensity nonuniformity (rms) for the 24-beam OMEGA system, as a function of focus, for three laser-beam intensity profiles: (a) quadratic, (b) flat-top, and (c) a recent experimentally obtained profile. In all cases an "asymptotic" nonuniformity level of 2% is achieved by defocusing the beam beyond tangential focus (8 target radii behind the target here).

profiles. Two of the profiles are: (1) quadratic, $I = I_0(1-r^2/r_0^2)$ and (2) flat-top, $I = I_0$ for $r < r_0$. The third is a recently obtained equivalent-target-plane profile from the GDL laser system,⁸ shown in Fig. 6. When these three profiles are compared, the main qualitative result is that the highest uniformity ($\sigma_{rms} < 1\%$) is obtained from a smoothly varying profile without sharp edges. The ideal quadratic shape need not be produced directly by the laser, but can be created in the target plane by the final focusing elements. Note that beyond tangential focus (corresponding to 8 target radii, 8R, behind the target in Fig. 5) the uniformity is insensitive to the beam shape. All profiles converge to

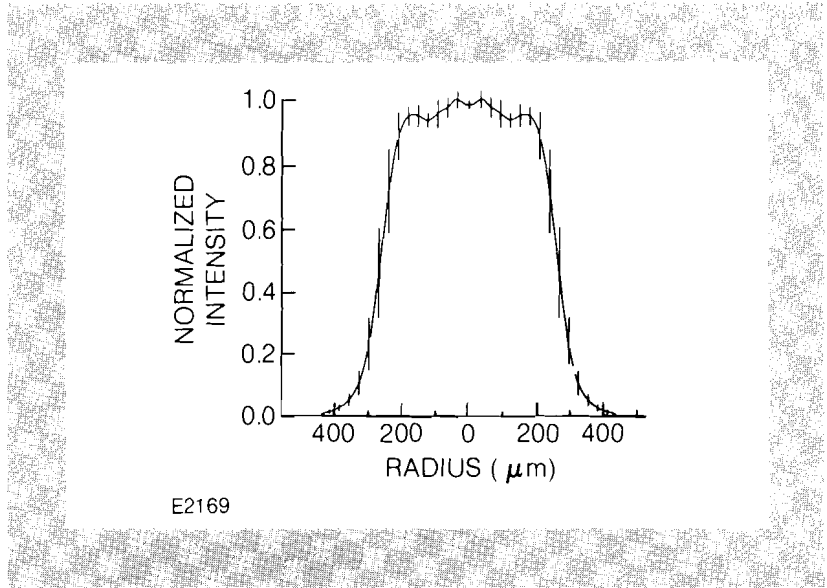


Fig. 6
Azimuthally averaged experimental intensity profile used for uniformity calculations. The vertical bars indicate the rms azimuthal variation around the average.

the same result ($\sigma_{rms} \sim 2\%$) because only the central part of the beam, which is similar for these profiles, reaches the target; the outer part is refracted. This 2% nonuniformity level does not require profiles very different from those presently available (although deviations from azimuthal symmetry have not yet been considered). The penalty for energy loss by refraction is relatively small in this example: the fractional absorption decreases by about 15% in defocusing from 7R to 12R.

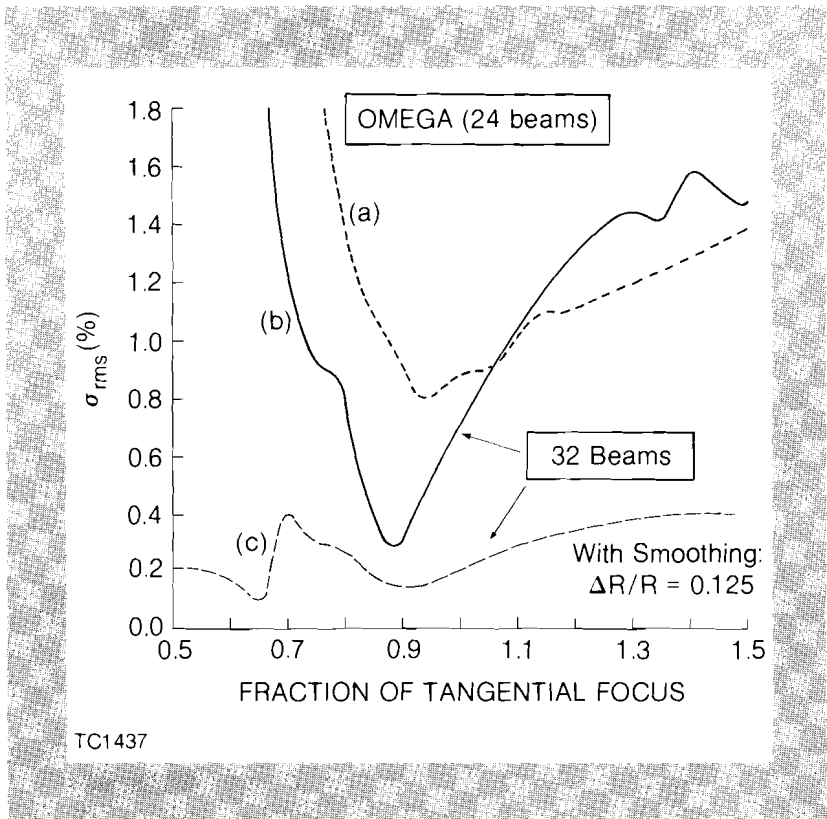


Fig. 7
Comparison of rms nonuniformity between (a) the 24-beam ($f/4$) laser system and (b) the 32-beam ($f/20$) system using a quadratic beam profile. Including moderate thermal smoothing (corresponding to $\Delta R/R = 0.125$), curve (c) is obtained for the 32-beam system.

The 24-beam ($f/4$) system is compared with the 32-beam ($f/20$) system in Fig. 7 using the quadratic profile. (Here the focus parameter should be multiplied by twice the f -number to obtain target radii; tangential focus equals 1 in these units.) There is a decrease in nonuniformity by a factor of 2 over a small focal range for the 32-beam system. This improvement is the result of higher geometrical symmetry, and it is particularly impressive since the solid angle subtended by the lenses is only 0.5%, compared with 15% for the 24-beam system.

This high degree of uniformity ($\sigma_{rms} < 1\%$) is obtained over a limited focal region. It is difficult to remain in this region during the entire laser-fusion implosion, as the focus parameter will be constantly changing. For short-wavelength irradiation the critical surface moves inward, so that the focal length, expressed in units of the instantaneous target radius, increases. One strategy is to focus so that the highest uniformity is obtained initially. At later times the nonuniformity will increase, but the target plasma will by then have expanded, and additional thermal smoothing of the short-wavelength nonuniformities may then be permitted.

Thermal Smoothing

While the calculations presented above give the nonuniformity in the absorption region, it is the nonuniformity at the ablation surface which determines the implosion nonuniformity. Improved symmetry at the ablation surface will result from thermal smoothing, an effect which may be estimated by multiplying each of the σ_ℓ of Eq. (4) by a classical attenuation factor⁹ of $\exp(-\ell\Delta R/R)$, where $\Delta R/R$ is the fractional separation of the critical and ablation surfaces. Clearly the short-wavelength nonuniformities (large ℓ) will be attenuated the most. A value of $\Delta R/R = 0.125$, characteristic of irradiation with $0.35\text{-}\mu\text{m}$ light, has been used; this leads to significant attenuation of modes with $\ell > 8$.

Typical results including smoothing are shown in the dashed curves of Figs. 5 and 7. In Fig. 5, σ_{rms} is reduced to below 1% for focusing beyond $10R$ for the experimental beam profile. Near-term experiments may therefore proceed with a relatively high uniformity, in parallel with the development of a beam-shaping capability. For future experiments with a 32-beam system and a quadratic beam profile, the dashed curve (c) of Fig. 7 shows that moderate thermal smoothing will lead to values of σ_{rms} below 0.4% over a broad focusing range.

Summary

The uniformity of laser-energy deposition on laser-fusion targets has been analyzed using a spherical-harmonic decomposition of the deposition pattern. It has been found that the contribution of each mode to the nonuniformity can be factored into two terms, one depending only on the geometrical orientation of the laser beams, and the other depending on details of the ray trajectories for only a single beam. The geometrical symmetry of the laser system effectively eliminates the longer-wavelength nonuniformities, and the shorter spatial wavelengths may be partially "tuned out" by varying the focus of the beam and its radial intensity profile.

Levels of nonuniformity less than 1% have been found at the critical surface. The nonuniformity may be reduced even further by lateral thermal transport as heat flows from the critical surface to the ablation surface. Even with the small separation between these surfaces expected for short-wavelength laser irradiation (0.35 μm), adequate thermal smoothing is possible due to the relatively small spatial wavelengths of the nonuniformities.

Finally, it has been shown that high uniformity can be obtained using the high-f-number optics (subtending less than 2% of the total solid angle) that will be required for future fusion reactors.

REFERENCES

1. J. H. Nuckolls, L. Wood, A. Thiessen, and G. Zimmerman, *Nature* **239**, 139 (1972).
2. W. C. Mead and J. D. Lindl, LLNL Report UCRL-78459 (1976).
3. M. H. Emery, J. H. Orens, J. H. Gardner, and J. P. Boris, *Phys. Rev. Lett.* **48**, 253 (1982).
4. R. G. Evans, A. J. Bennett, and G. J. Pert, *J. Phys. D* **15**, 1673 (1982).
5. S. Skupsky and K. Lee, LLE Report 137, submitted for publication to *Journal of Applied Physics*.
6. M. J. Monsler, J. Hovingh, D. L. Cook, T. G. Frank, and G. A. Moses, *Nucl. Technol./Fusion* **1**, 302 (1981).
7. C. E. Max, C. F. McKee, and W. C. Mead, *Phys. Fluids* **23**, 1620 (1980).
8. LLE Review **12**, 5 (1982).
9. S. E. Bodner, *J. Fusion Energy* **1**, 221 (1981).

2.B Thermal Transport Measurements on OMEGA

Transport experiments have been conducted on the 24-beam OMEGA laser system under conditions of uniform spherical irradiation. Thermal transport in spherical geometry has been found to differ from transport under comparable single-beam target-irradiation conditions, and cannot be described in terms of a flux-inhibited model. We have found on OMEGA that electrons in the tail of the thermal velocity distribution deposit energy deep into the target, leading to a temperature profile which is less steep than predicted by a flux-inhibited model.

Thermal transport is one of the crucial processes affecting target performance in laser fusion. Many experiments to determine transport have been conducted in single-beam irradiation geometry; on GDL, for example, inhibited transport consistent with a flux limiter of 0.03-0.05 was found for 0.35- μm irradiation.¹ Recent spherical irradiation experiments at the Rutherford Laboratory² have, however, indicated less inhibited transport than most single-beam experiments, and suggested a higher value of 0.1 for the flux limiter.

Thermal transport can be deduced from "burn-through" measurements on simple layered targets comprising a layer of ablator material (e.g., plastic) coated onto a substrate. The intensity of appropriate x-ray lines from the substrate layer is measured for various overcoat-layer thicknesses and comparison is made with code predictions. A high degree of uniformity is essential when comparing experimental transport results with a one-dimensional code. This is available on OMEGA: by focusing at a point which is about eight target radii behind the target center (tangential focus), the resulting rms intensity nonuniformity of the 24 overlapping beams is smaller than 6%.

The targets used in this study were thin glass shells of diameter $\sim 400 \mu\text{m}$, coated with a $2\text{-}\mu\text{m}$ -thick copper layer, a "substrate" layer (Al, Ni, or Ti), and varying thicknesses of ablator material (parlyene). The copper coating made the target sufficiently massive to ensure that the transport issue would not be complicated by hydrodynamic motion. The substrate layer provided signature x-ray emission, measured with x-ray Bragg spectrographs and spectrally resolving x-ray streak cameras.

Figure 8 shows burn-through curves for various incident (and absorbed) irradiances. The intensity of the $2p\text{-}1s$ line of Al^{+12} at 1.73 keV

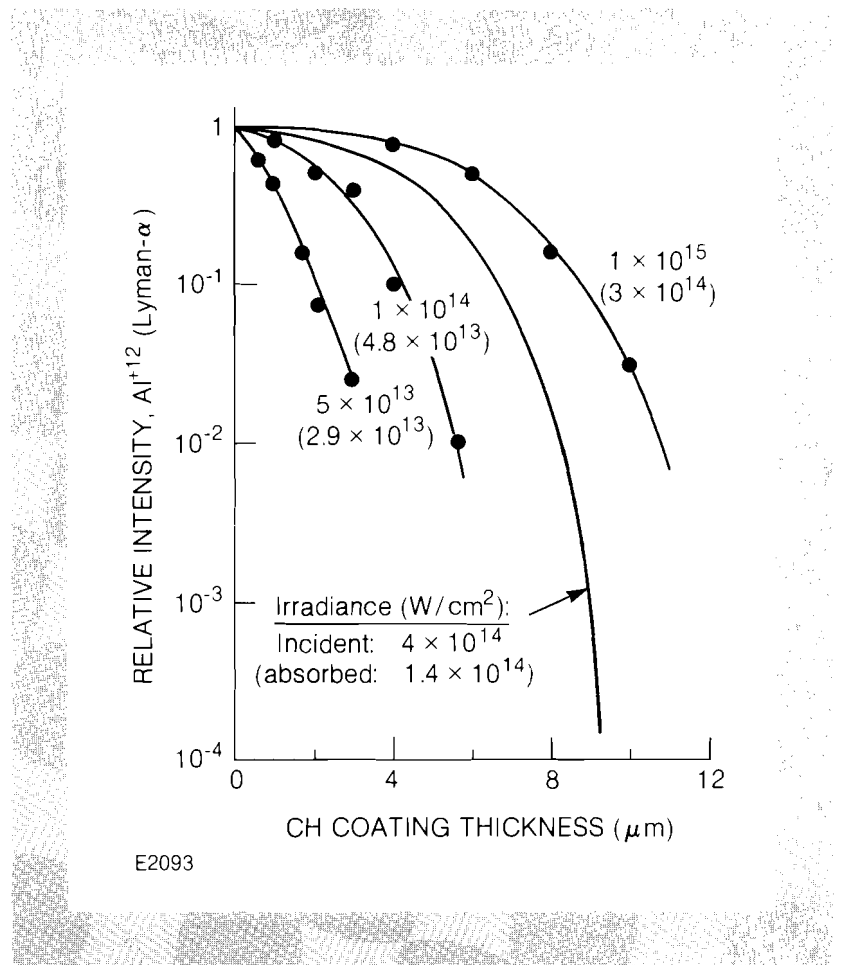
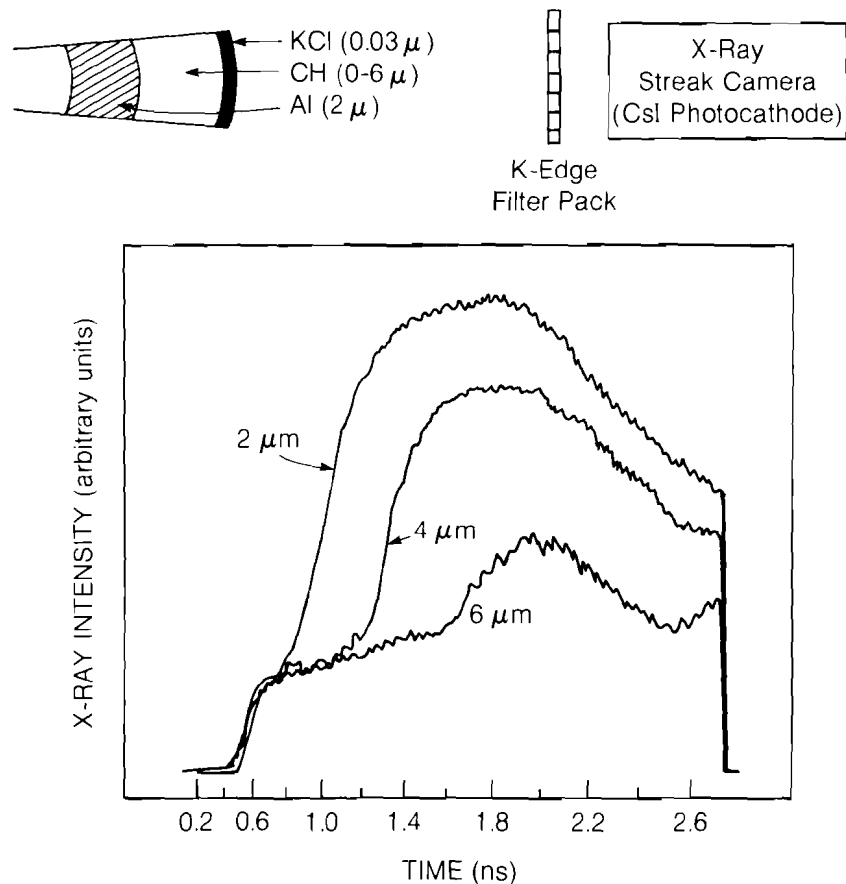


Fig. 8
Transport is studied by measuring the x-ray signal from an aluminum substrate coated with various thicknesses of parlyene (CH). Greater thicknesses of parlyene are burnt through at higher intensities. The mass-ablation rate may be estimated by dividing the burn depth by the laser pulse width.

Fig. 9

X-ray streak traces for different CH coating thicknesses, at 4×10^{14} W/cm². The filter in front of the camera selects the photon energy range $\sim 2-2.8$ keV which includes the aluminum line used in Fig. 8. The first rise in intensity (at 0.5 ns) marks the heating of the KCl surface layer. The second rise is due to penetration into the aluminum substrate. The mass-ablation rate may be estimated directly from the times of onset of this second rise in successive traces.

is plotted against the thickness of the parylene coating. For each case, the "penetration depth" is about three times larger than predicted by the one-dimensional laser fusion code *LILAC* for a flux limiter $f = 0.03-0.05$; it is comparable to what is predicted for no flux limitation ($f = 0.65$), but in this case the calculated absorption fraction is too high by a factor of two. The fact that no intensity threshold is observed for this departure from theory suggests that this discrepancy is not caused by an instability, such as filamentation which would lead to nonuniform heat penetration. This conclusion is supported by x-ray streak-camera measurements (Fig. 9) which show that the sharp rise in intensity (due to penetration into the substrate) occurs progressively later in time for thicker parylene thicknesses. With filamentation, we would expect this rise to occur near the peak of the pulse; in contrast, for the 6- μ m case this rise occurs when the laser pulse is practically over.



E2233

Since the present results for uniform, spherical irradiation are markedly different from most reported results for single-beam, plane-target irradiation, we have compared the uniform and nonuniform irradiation of spherical targets at the same incident irradiance (see Fig. 10). We used two additional geometries: (a) one single beam (of the 24 OMEGA beams) was focused to a 150- μm -diameter spot on spherical targets, and (b) all 24 beams were focused to small discrete spots, of diameter 70 μm , on the surfaces of spherical targets. The incident irradiance in all these cases was adjusted to the same approximate value of $4 \times 10^{14} \text{ W/cm}^2$. The nonuniform irradiance curve in Fig. 10 fits both cases (a) and (b), and agrees with a LILAC prediction assuming $f=0.03$ and spherical symmetry. We are led to conclude that this agreement is fortuitous: there must be some two-dimensional effects which manifest themselves as an effective flux inhibition.

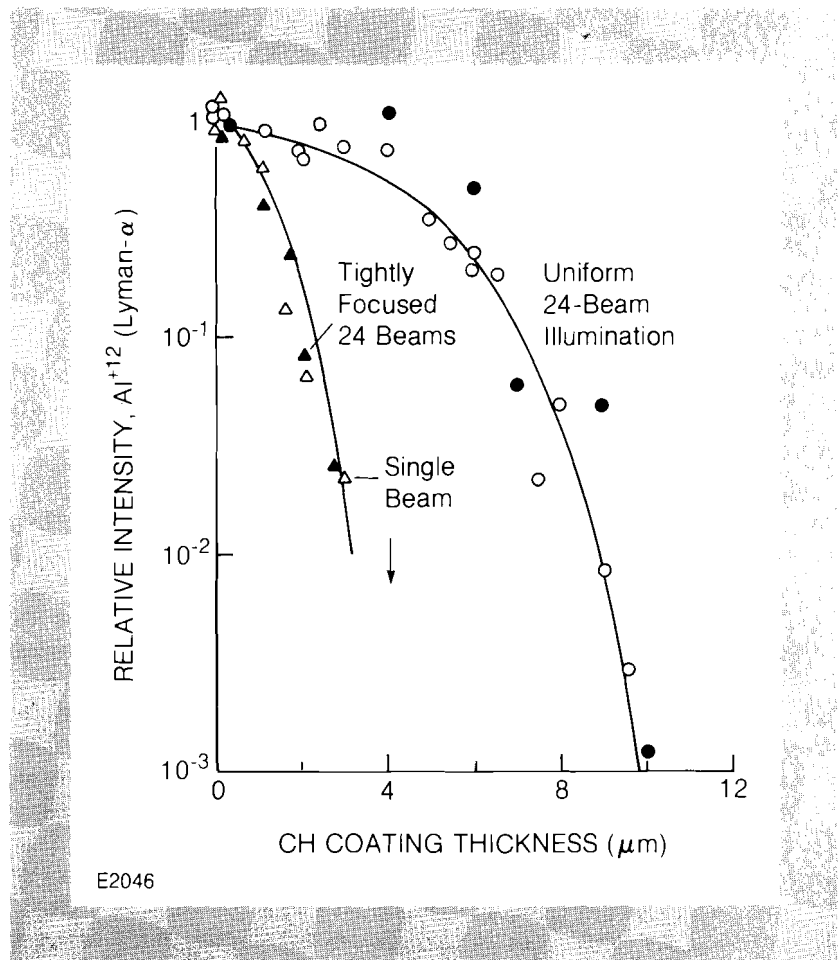
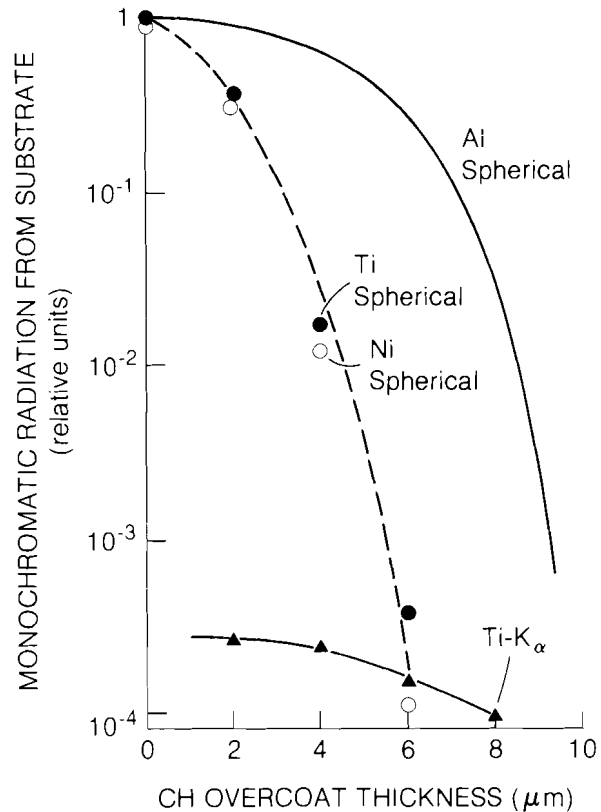


Fig. 10
Comparison of burn-through for uniform and nonuniform irradiation of spherical targets. In each case the target was CH coated on aluminum, and the irradiance was approximately $4 \times 10^{14} \text{ W/cm}^2$. The arrow indicates a coating thickness for which the x-ray signal was below the threshold for detectability. The different curves were separately normalized to 1. The full and empty circles pertain to two separate series of experiments, demonstrating the reproducibility of the results.

Mapping of the heat-front temperature profile is essential to the understanding of transport in spherical geometry. We have extended these burn-through measurements using higher-atomic-number substrates, titanium and nickel. Figure 11 summarizes the results for an incident irradiance of $4 \times 10^{14} \text{ W/cm}^2$. The aluminum line at 1.73 keV probes temperature contours near 400 eV, while the corresponding titanium line at 4.75 keV and the nickel line at 7.8 keV probe higher temperatures, near 1 keV and 1.5 keV respectively. The marked dif-

Fig. 11

Burn-through of parylene coating for substrates of different Z (aluminum, titanium, and nickel), at $4 \times 10^{14} \text{ W/cm}^2$. The higher- Z elements indicate a smaller burn depth, since the x-ray lines used are excited at higher temperatures. The titanium K_α yield, indicative of the preheat of cold material by fast electrons, is also shown.



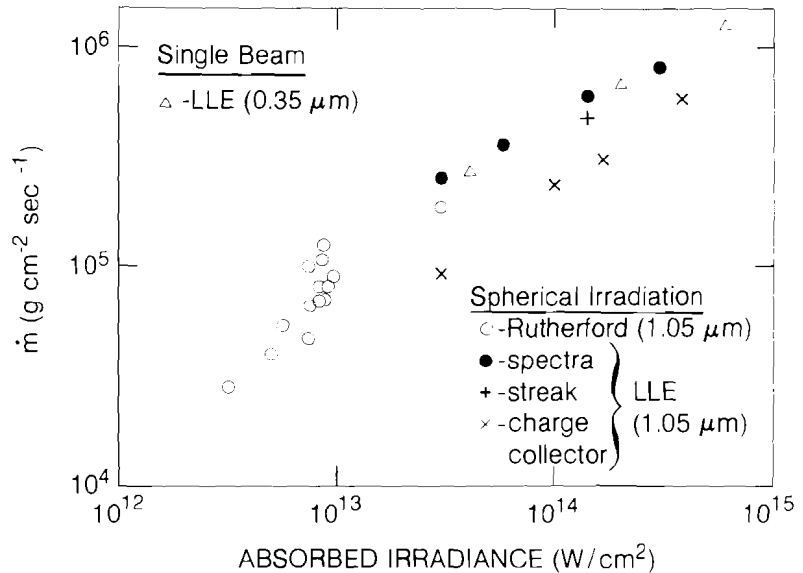
E2107

ference between the low- Z and high- Z burn-through curves is evidence of a very gradual temperature fall at the heat front. It shows the inapplicability of the flux-limited model (with any f), or even the classical uninhibited model; both these models predict a very steep heat front, and a burn-through curve almost independent of substrate material. There is probably penetration of only a "foot" of relatively low temperature ahead of the heat front into the higher-density, deeper target layers. The rest of the heat front may still be described by flux-inhibited transport.

Figure 11 also shows the intensity of K_α lines from the high- Z substrate which are indicative of preheat by fast electrons. Using the absolute magnitude of the K_α line intensities, we would estimate³ that only about 0.7% of the absorbed energy at 10^{15} W/cm^2 is deposited as fast-electron preheat. This, however, may be misleading: resonance-absorption electrons which move inwards from the critical layer encounter a layer of thickness of the order of their range which is already heated by the penetrating "foot" of the heat front. The emission of K_α radiation, which requires cold material, is therefore thwarted. In other words, the preheat is actually higher than deduced from the K_α line.

Burn-through curves (see Fig. 8) can be used to obtain the peak

mass-ablation rate. The total mass ablated is taken as that corresponding to the maximum penetration of the aluminum emission curves in Fig. 8. After dividing by the pulse width and applying a small correction factor⁴ we arrive at the results shown in Fig. 12 (solid points).



E2234

Fig. 12 Comparison of mass-ablation rates as a function of absorbed irradiance. Results marked by solid circles were obtained from the burn-through curves in Fig. 8; + —by streak traces (see Fig. 9); x—by charge-collector signals. Results obtained at LLE and the Rutherford Laboratory are consistent.

The streak-camera results (Fig. 9) allow the mass-ablation rate to be estimated directly by taking the time difference of the onset of the second rise in successive traces. For example, for the 2- μm and 4- μm coating thicknesses, this onset occurs near 0.8 and 1.2 ns, respectively.

The mass-ablation rate can alternatively be determined from the average ion velocity as measured by charge collectors. If E_a is the absorbed energy per unit area, V the ion expansion velocity, and Δt the pulse width, the mass-ablation rate is given approximately by $\dot{m} = 2E_a/V^2\Delta t$, where V^2 is averaged over the distribution. The mass-ablation rate so derived is shown in Fig. 12 to be consistently lower than that derived spectroscopically. This indicates that the deep penetration of lower temperature contours does not contribute to mass ablation and hence to drive efficiency as much as if the entire heat front had penetrated to the same depth.

For comparison, we also show in Fig. 12 results obtained at the Rutherford Laboratory using spherical irradiation at $\lambda = 1.05 \mu\text{m}$,² and results reported earlier by us using single-beam irradiation at $\lambda = 0.35 \mu\text{m}$.¹ Since \dot{m} for spherical irradiation was found to be about the same at different laser wavelengths (for the same absorbed irradiance),² we can expect from Fig. 12 that for $\lambda = 0.35 \mu\text{m}$, \dot{m} would be

about the same for single-beam and for spherical irradiation. This contrasts with our finding for 1.05- μm irradiation that \dot{m} for spherical irradiation is about *three times higher* than most reported results for the single-beam case.

These observations provide an improved understanding of transport. Nonlocal heating results in a more gradual temperature drop into the target which is consistent with the results of Fig. 11. This "smearing" of the heat front results from the longer mean free path of electrons in the tail of the thermal-electron velocity distribution. We expect these effects to diminish in importance as we move to shorter-wavelength irradiation because of the increased critical density (and, in addition, a lower temperature if different wavelengths are compared at the same absorbed irradiance).

In order to understand better the impact of the multi-energy-group nature of transport one needs to incorporate the equivalent of a Fokker-Planck treatment⁵ into a hydrodynamic code. This has been done using an approximation (a "hybrid" treatment) which greatly economizes computation time while preserving the essential multi-group, nonlocal character of transport. Another important consideration is that the excitation rates of the x-ray lines used are changed in the presence of non-Maxwellian electron distributions. Theoretical analysis of these experiments taking these developments into account is now in progress.

REFERENCES

1. B. Yaakobi, T. Boehly, P. Bourke, Y. Conturie, R. S. Craxton, J. Delettrez, J. M. Forsyth, R. D. Frankel, L. M. Goldman, R. L. McCrory, M. C. Richardson, W. Seka, D. Shvarts, and J. M. Soures, *Opt. Commun.* **39**, 175 (1981).
2. T. J. Goldsack, J. D. Kilkenny, B. J. MacGowan, P. F. Cunningham, C. L. S. Lewis, M. H. Key, and P. T. Rumsby, *Phys. Fluids* **25**, 1634 (1982).
3. B. Yaakobi, J. Delettrez, L. M. Goldman, R. L. McCrory, W. Seka, and J. M. Soures, *Opt. Commun.* **41**, 355 (1982).
4. Rutherford Laboratory Annual Report RL-81-040, Chap. 4.4 (1981).
5. A. R. Bell, R. G. Evans, and D. J. Nicholas, *Phys. Rev. Lett.* **46**, 243 (1981).

2.C High-Resolution Harmonic Photography on OMEGA

The study of harmonic emission from spherical targets irradiated by intense laser light is of interest for several reasons. Two-dimensional harmonic photography, particularly of the $2\omega_0$ and $3\omega_0/2$ emissions, has long been used as a signature of the critical (n_c) and quarter-critical ($n_c/4$) surfaces. The $2\omega_0$ emission is generally believed to originate from the critical density surface, as a second-order overtone

of the driving electric field during resonance absorption, and the $3\omega_0/2$ emission from the quarter-critical density surface due to the interaction between incident radiation at frequency ω_0 and plasma waves at $\omega_0/2$ generated by plasma instabilities such as the two-plasmon ($2\omega_{pe}$) instability.¹ Thus, two-dimensional photography of these harmonics permits the measurement of the excursions of both the critical and quarter-critical density surfaces during the irradiation of the target.²

Since both critical-density and quarter-critical-density phenomena are intensity sensitive, high-spatial-resolution harmonic photography may be used to give an indication of the overall uniformity of irradiation of targets under multi-beam illumination. In addition, analysis of the spectral and temporal characteristics of harmonic emission, particularly the $3\omega_0/2$ emission, shows considerable potential as a means of diagnosing the coronal electron temperature; this analysis also aids in the understanding of those processes which produce hot electrons deleterious to efficient target implosions.

Studies of the harmonic emission from spherical targets irradiated by the 1.053- μm , 24-beam OMEGA laser facility were performed with the instrumentation shown in Fig. 13. A high-resolution (2- μm) binocular camera system was used to obtain photographs of the second-harmonic and $3/2$ -harmonic emissions in a common viewing direction.

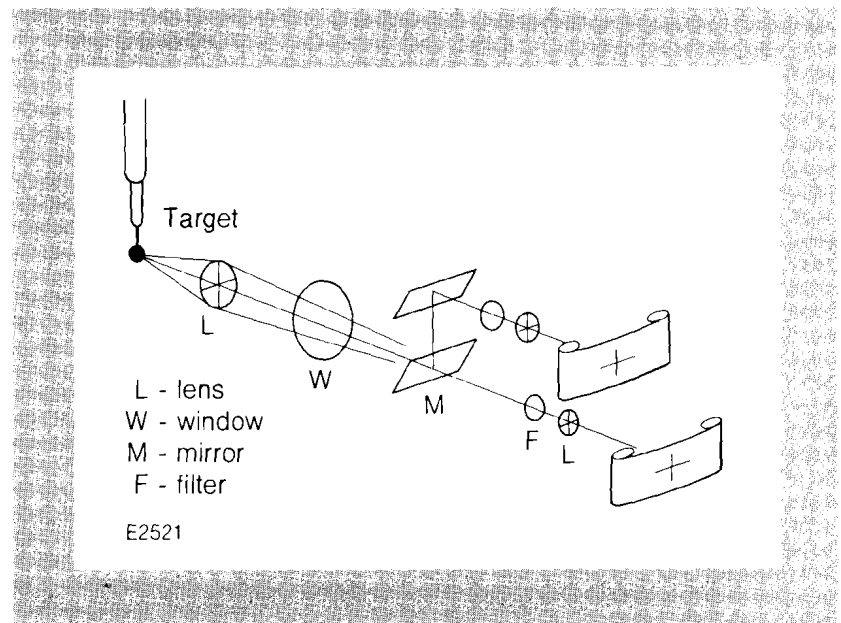


Fig. 13
Experimental setup on OMEGA used for the analysis of harmonic emission from spherically irradiated targets. This setup enables the target to be simultaneously photographed in two different wavelengths from the same direction.

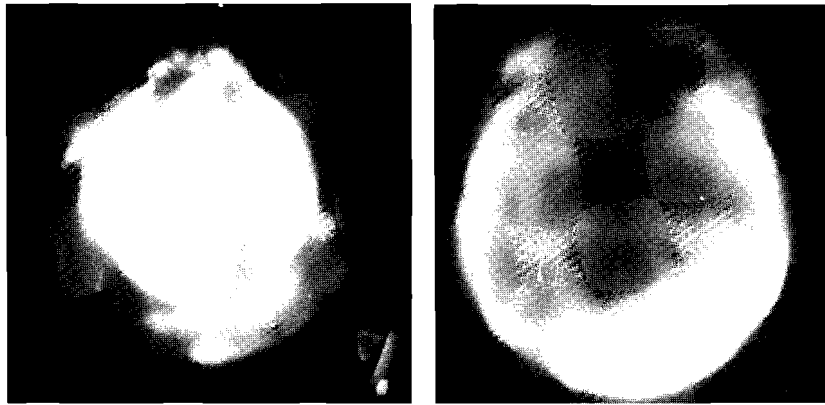
Typical photographs of the second-harmonic and the $3/2$ -harmonic emissions originating from a uniformly irradiated glass microballoon are shown in Fig. 14. This large-aspect-ratio target ($R/\Delta R \sim 200$), of 400- μm diameter and DT-filled, was irradiated uniformly with a 1-ns pulse at an average intensity of 3.6×10^{14} W/cm². The three photographs show the original target size and the $2\omega_0$ and $3\omega_0/2$ emissions on a common spatial scale.

Several features in these harmonic-emission photographs are apparent. The principal component of the second harmonic originates

TARGET IMAGE

IMAGE OF $2\omega_0$ EMISSION

IMAGE OF $3\omega_0/2$ EMISSION

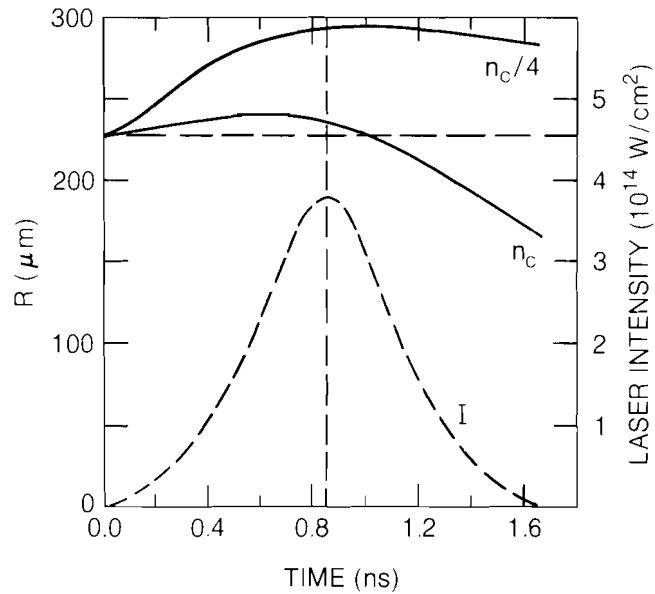


Shot 7141
E1768

Fig. 14
Spatially resolved $2\omega_0$ - and $3\omega_0/2$ -harmonic emission from a 420- μm -diameter, 1- μm -wall-thickness, DT-filled glass microballoon irradiated uniformly with 24 beams at an intensity of $3.6 \times 10^{14} \text{ W/cm}^2$ for 1 ns. The outer component of the second-harmonic emission is believed to originate from the quarter-critical region.

from a region similar in diameter to that of the original target. The $3\omega_0/2$ emission, on the other hand, originates from a region considerably greater in extent and exhibits a fairly sharp outer boundary. In both harmonics, the perturbing effect of the stalk support on the symmetry of the underdense corona is clearly visible.

The spatial scales of the second-harmonic and 3/2-harmonic emissions are in broad agreement with what is expected on the basis of one-dimensional *L/LAC* code calculations. This is illustrated in Fig. 15,



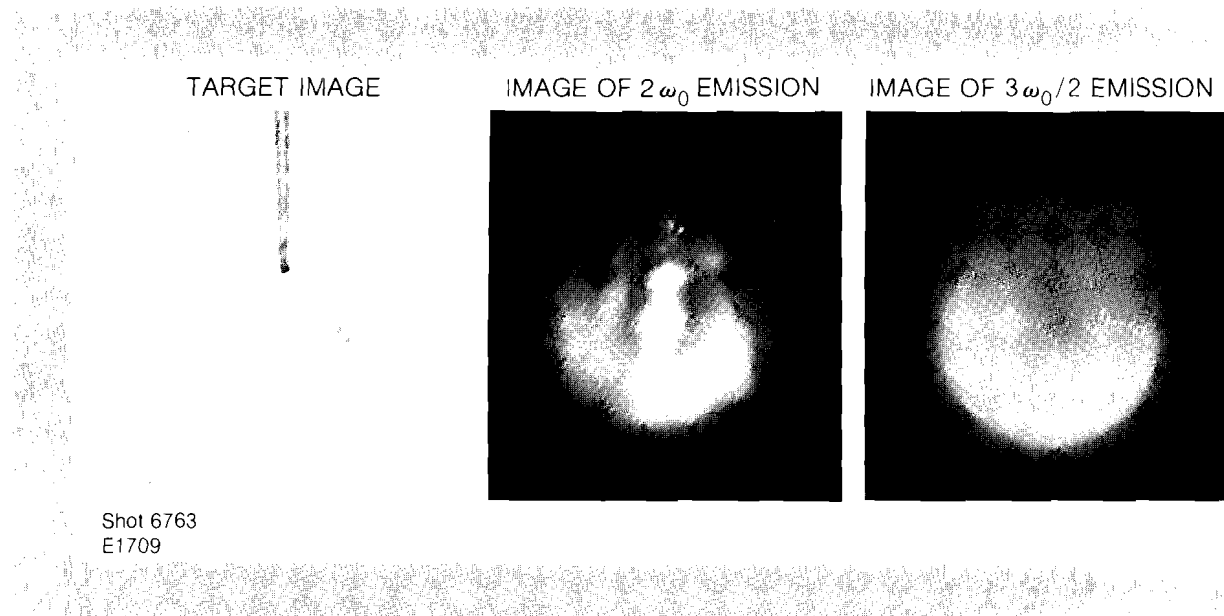
E2522

Fig. 15
One-dimensional code predictions of the trajectories of the n_c and $n_c/4$ surfaces for a 450- μm -diameter, 1- μm -wall-thickness, DT-filled glass microballoon irradiated at $4 \times 10^{14} \text{ W/cm}^2$. The dashed curve indicates the time history of the incident laser intensity (relative to the initial target radius).

which shows a simulation of the trajectories of the critical and quarter-critical densities throughout the duration of the laser pulse. The irradiation conditions are similar to those that were used in obtaining the data in Fig. 14. The simulation assumes absorption on a self-consistent density profile, principally by inverse bremsstrahlung, with a 10% deposition of the radiation reaching the critical surface into fast electrons having a temperature prescribed by the Livermore model of resonance absorption.³ In addition, the simulation utilizes a flux-limited prescription for thermal transport with a value of $f = 0.05$. As can be seen, the simulation predicts little excursion of the critical surface during the laser pulse while showing an excursion of approximately $100 \mu\text{m}$ for the quarter-critical region. This is in close agreement with the spatial scales of the harmonic emission.

Figure 14 shows that, in addition to the predominant second-harmonic emission from a region of the target equivalent in size to the original target diameter, there is evidence for a secondary component having a spatial scale and general morphology similar to that of the $3/2$ -harmonic emission. This would suggest the generation of $2\omega_0$ emission from the $n_c/4$ region, an observation that has not previously been made. Some additional experiments have been performed to characterize further this secondary component of the second-harmonic emission. Figure 16 shows harmonic photographs of a small target irradiated with 1.3-ns pulses at an intensity of $1.5 \times 10^{15} \text{ W/cm}^2$. Under these conditions the penumbral second-harmonic emission is of greater intensity than the emission originating from the critical-density region and still displays spatial characteristics similar to the $3\omega_0/2$ emission.

Fig. 16
Variation of spatial characteristics of harmonic emission with irradiation intensity. This $192\text{-}\mu\text{m}$ -diameter glass-microballoon target was uniformly irradiated with an intensity of $1.5 \times 10^{15} \text{ W/cm}^2$. These harmonic images should be compared with those of Fig. 14.



A photographic analysis of the $5\omega_0/2$ -harmonic emission at 4230 \AA has also been made. Figure 17 shows a typical image of the $5\omega_0/2$ emission from a $\sim 400\text{-}\mu\text{m}$ -diameter, $1\text{-}\mu\text{m}$ -thick DT-filled glass microballoon, irradiated uniformly at $4 \times 10^{14} \text{ W/cm}^2$. This emission also appears to originate from the quarter-critical region.

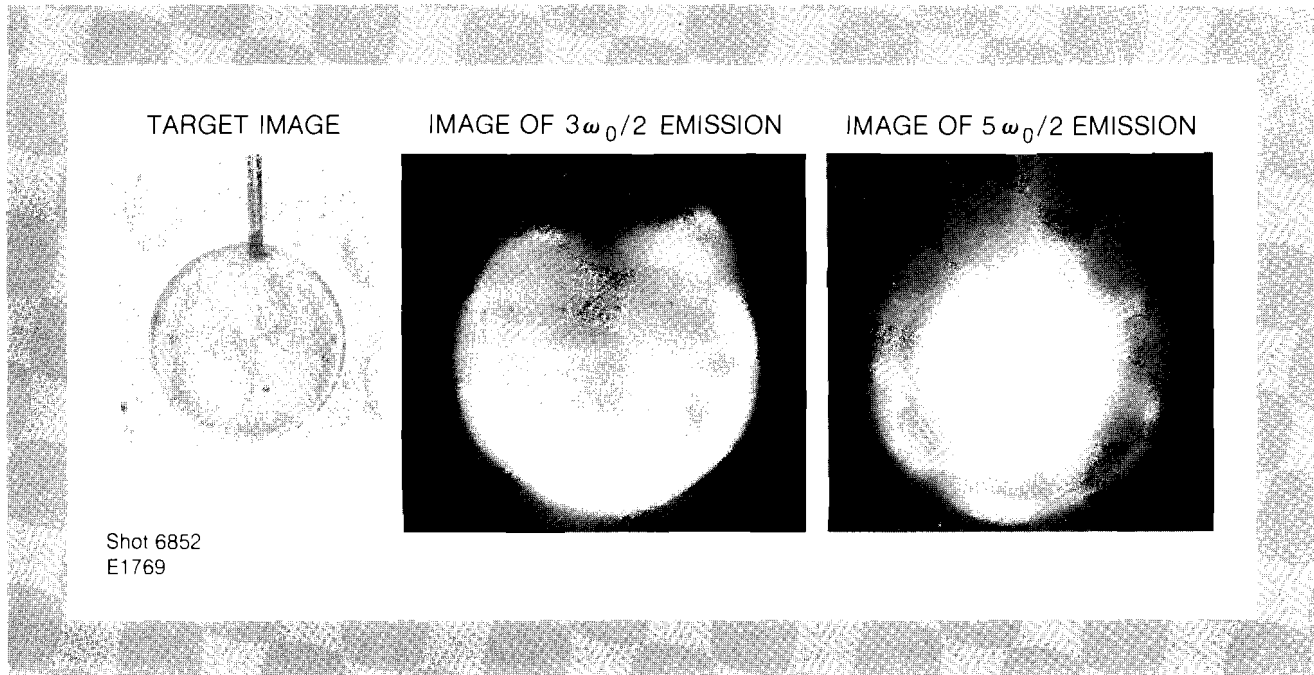


Fig. 17
 Comparison of the spatial distribution of the $3\omega_0/2$ - and $5\omega_0/2$ -harmonic emissions from a uniformly irradiated 415- μm -diameter, 1- μm wall thickness, DT-filled glass microballoon irradiated at 4×10^{14} W/cm². The $5\omega_0/2$ emission also appears to originate from the quarter-critical region.

Photography of the extent of the harmonic emission can also be used to identify nonuniform and microstructural effects in the underdense corona. This is illustrated in Fig. 18 which shows the harmonic emission from a 235- μm -diameter glass microballoon overcoated with Cu (2 μm), Al (2 μm), and CH (10 μm). Targets of this type were recently used in analyzing thermal transport in spherical geometry (see Section 2.B in this issue). In general, targets having a low-Z outer layer displayed interesting features in the underdense corona. In particular, the 3/2-harmonic emission showed strong evidence for small-scale microstructures at the quarter-critical surface, as can be seen from Fig. 18. Although this structure is clearly visible at the quarter-critical surface, the second-harmonic photograph taken from the same direction shows little evidence for similar structure at the critical-density surface.

Summary

Photographic analysis of the harmonic emission from spherical targets irradiated with the multi-beam OMEGA system has led to many interesting findings. The excursions of the critical and quarter-critical surfaces, as determined from $2\omega_0$ and $3\omega_0/2$ emissions respectively, are in broad agreement with one-dimensional code calculations assuming inverse-bremsstrahlung absorption and a flux-limited thermal transport model (with $f = 0.05$).

The study of the spatial distribution of the harmonic emission has been a valuable addition to the ongoing studies aimed at estimating the level of irradiation uniformity achieved on OMEGA.⁴ Finally, the spectral and temporal characteristics of the harmonic emission have the potential for increasing our understanding of instability phenomena occurring in the underdense region. These features of the harmonic emission have been studied in greater detail and will be described in a forthcoming issue of the LLE Review.

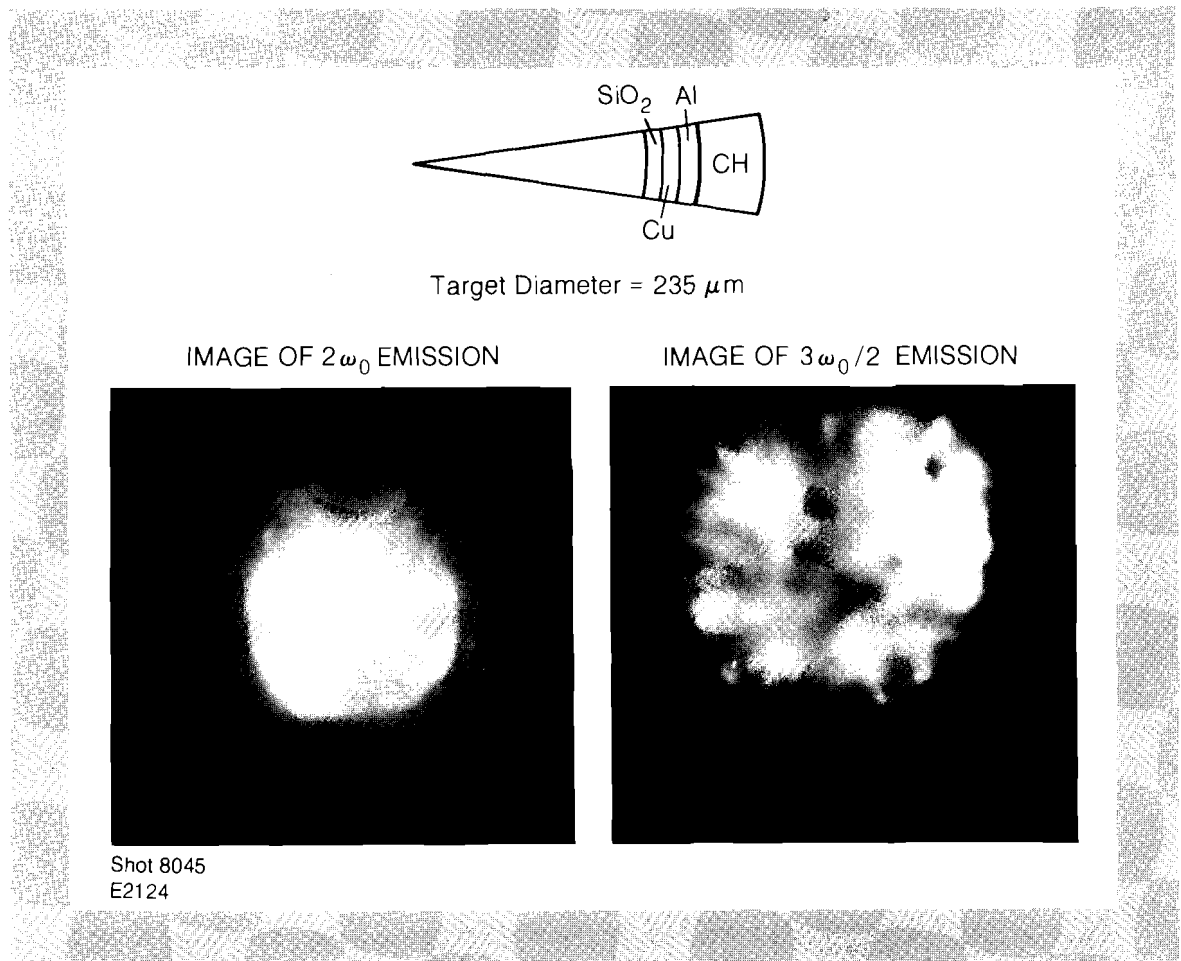


Fig. 18
Observation of small-scale structure in the harmonic emission from a uniformly irradiated low-Z shell. The origin of this structure is not understood at present.

REFERENCES

1. S. Jackel, B. Perry, and M. Lubin, *Phys. Rev. Lett.* **37**, 95 (1976).
2. J. Rizzo, S. Letzring, D. Villeneuve, M. C. Richardson, G. Gregory, R. S. Craxton, J. Delettrez, K. Lee, and R. Hutchison, *Proceedings of the Second Conference on Lasers and Electro-Optics (CLEO)*, Phoenix, AZ (1982).
3. K. Estabrook and W. L. Kruer, *Phys. Rev. Lett.* **40**, 42 (1978).
4. M. C. Richardson *et al.*, *Proceedings of the Ninth Int. Conf. Plasma Physics and Controlled Thermonuclear Fusion Research (IAEA)*, Baltimore, MD (1982) (to be published).

2.D Continuum X-Ray Spectra from UV- and IR-Laser-Produced Plasmas

A major reason for the interest in short-wavelength ($\lambda \leq 0.5 \mu\text{m}$) laser fusion is the fact that absorption occurs primarily through inverse bremsstrahlung rather than through resonance absorption, thus avoiding one of the major sources of superthermal electrons. Because

of their long mean free path, these electrons can preheat the target core and tamper, thereby reducing the efficiency with which targets can be compressed.

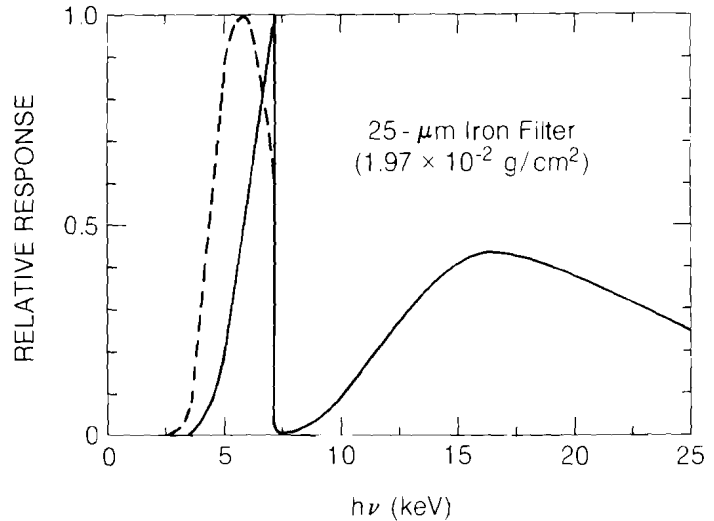
Parametric instabilities occurring in the underdense plasma may also produce fast electrons,^{1,2} and we have previously reported observations of these instabilities in experiments conducted on the 0.35- μm GDL facility.³ In order to assess the importance of parametric instabilities as sources of fast electrons, we have measured the x-ray continuum emitted from UV-generated plasmas on GDL. The x-ray continuum, produced by electrons in the plasma as they slow down, provides a measure of the mean electron velocity (temperature) and total energy of any superthermal electron components in the plasma. We find that while there is no component attributable to resonance absorption, there is a very high temperature (20-30 keV) component which we attribute to the two-plasmon ($2\omega_p$) instability. The threshold intensity for this component was found to be approximately 2×10^{14} W/cm², and saturation appeared to occur above approximately 4×10^{14} W/cm². The energy in this component was less than 0.1% of the incident laser energy.

Experiment

The targets used for these experiments were planar plastic (CH) and effectively of infinite mass. The intensity on target was varied by changing both the laser energy and the focal position. Focal-spot diameters ranged from 100 to 300 μm . The x-ray continuum was measured using K-edge-filter detectors. These detectors consist essentially of a foil absorber mounted in front of an x-ray detector. They are so named because they utilize the jump in x-ray absorption which occurs in the foil when the energy of an incident x ray is sufficient to remove an electron from the K-shell (innermost shell) of an atom in the foil. The response function for a typical K-edge filtered detector is shown in Fig. 19. While the peak response occurs in a narrow band just below the K-edge energy of the filter, there is also a broad low-level sensitivity at energies above the K-edge. If the measured x-ray spectrum is sufficiently cold, the effective response tends to be localized just below the K-edge as shown by the dashed curve in Fig. 19.

Nine silicon PIN diodes and six NaI scintillators coupled to photomultiplier tubes (PMT's) were utilized as x-ray detectors. Lead shields and collimators were incorporated in the detector arrays to ensure that only x rays produced in the target reached the detectors. The PMT detectors were calibrated using Am^{241} and Co^{60} nuclear sources; the sensitivity of silicon is well known. The signals from the detectors were integrated and recorded using gated analog-to-digital converters and a computer-controlled data-acquisition system. The signals were also monitored with oscilloscopes to check for detector saturation and to monitor the signal-to-noise ratio.

Reduction of the data from the K-edge-filter detector system is complicated by the fact that the response of the detectors is not truly narrow-band. This requires that the x-ray spectrum be obtained self-



E2408

Fig. 19
 Response function of a typical K-edge detector (solid line). The effective response obtained with a 1-keV temperature spectrum is also shown (dashed line).

consistently over the entire range of energy covered by the full detector system. To do this we use a multi-Maxwellian model for the spectrum and assume that the spectrum can be approximated by:

$$\frac{dE}{d(h\nu)} = \sum_{j=1}^K N_j \exp(-h\nu/T_j) \quad (1)$$

In this expression, N_j and T_j are parameters which are determined through a least-squares fit to the measured data. If the electron distribution actually consists of K Maxwellians, then the parameter T_j represents the temperature of the j 'th component. Since the measurement is both time- and space-integrated and the actual electron distribution is not known, the T_j should only be loosely interpreted as representing actual electron temperatures. Our choice of spectral model is motivated by several considerations. Numerical simulations of resonance absorption⁴ and parametric instabilities⁵ predict electron distributions which are approximately Maxwellian. This model also permits the spectrum to be described by a small number of physically useful parameters. Finally, we find that for a suitable choice of K , we obtain good fits to the data.

We may obtain the total energy, E_j , in a superthermal electron component from the x-ray spectrum using the relation:

$$E_j = N_j / (1.6 \times 10^{10} \langle Z^2 \rangle / \langle Z \rangle) \text{ (joules)} .$$

This result, which was derived by Brueckner,⁶ assumes that a fast electron loses its energy primarily through collisions with a cold background plasma, and neglects losses to fast ions and processes which could enhance the radiation rate. It depends only weakly on

plasma conditions and is relatively insensitive to the actual electron distribution.

Results

A typical spectrum is shown in Fig. 20. The solid curve is obtained by using the model and procedure previously described. In order to evaluate the quality of fit and approximate range of x-ray energies measured by a particular detector, we first perform the least-squares fit and then plot the data at the locations given by:

$$\left(h\nu', \frac{S_{\text{meas}}}{S_{\text{calc}}} \frac{dE}{dh\nu} \Big|_{h\nu'} \right)$$

where S_{meas} is the measured signal and S_{calc} is the signal calculated from the best-fit spectrum $dE/dh\nu$. The frequency ν' is chosen such that half of S_{calc} is produced by x rays with energy less than $h\nu'$. The figure illustrates a two-Maxwellian fit. We will refer to the hottest component (the segment with flattest slope) as the "superhot" component, while the other component will be referred to as cold. The component produced by resonance absorption, which is conventionally referred to as hot, is not seen in these 0.35- μm experiments. Here we are primarily interested in the superhot component; the cold component, produced in the dense plasma near the ablation surface, will not be further mentioned.

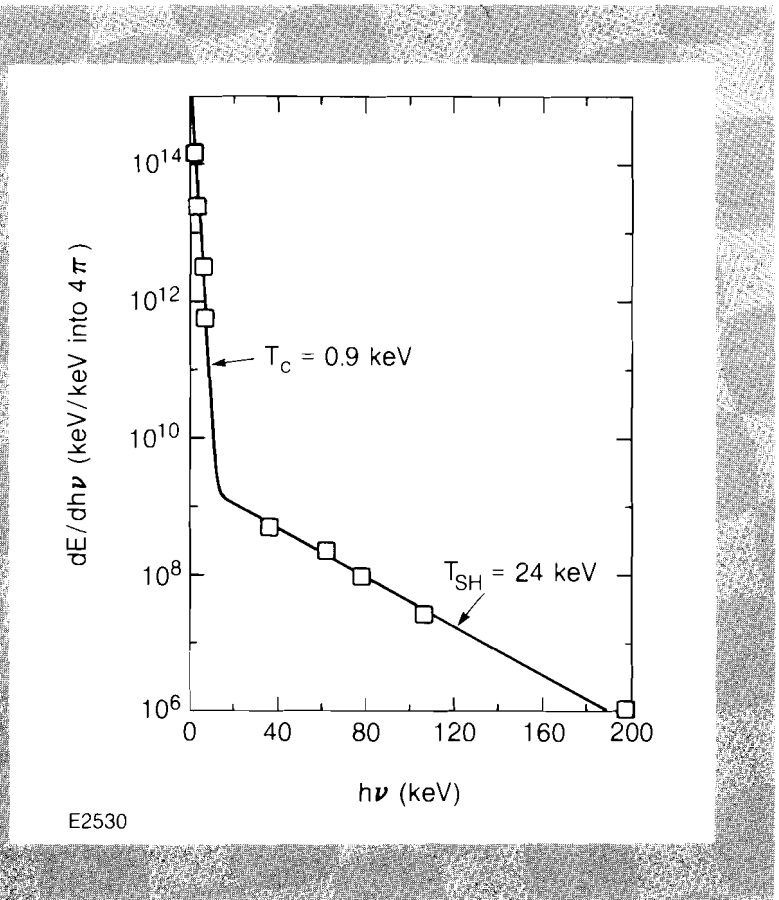


Fig. 20
Typical two-Maxwellian spectrum obtained with 0.35- μm irradiation. The curve is obtained using the least-squares fitting procedure outlined in the text. The data points are plotted only after the fit is obtained, and are intended to illustrate the quality of the fit and the approximate x-ray energies sampled.

Figure 21 shows the measured superhot temperature as a function of intensity. Results obtained with both 0.5-ns and 1-ns laser pulse lengths are shown. A slow $I^{0.2}$ scaling of temperature with intensity is

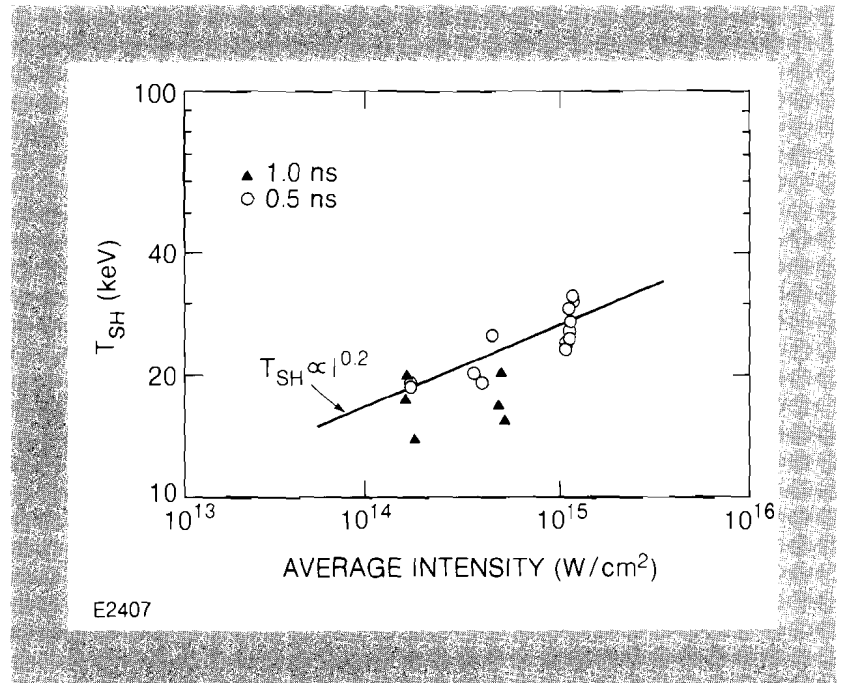


Fig. 21
Superhot temperature as a function of incident intensity at 0.35 μm . The solid line is a fit to the 0.5-ns data.

evident. Figure 22 shows the dependence of the superhot electron energy on the incident intensity. We note a rapid increase above approximately $1.5 \times 10^{14} \text{ W/cm}^2$ and a subsequent saturation. This behavior is very similar to that observed for the $\omega_0/2$ radiation emitted by these plasmas, which has been correlated with the $2\omega_p$ instability at quarter-critical.³ Because of the close correlation between the

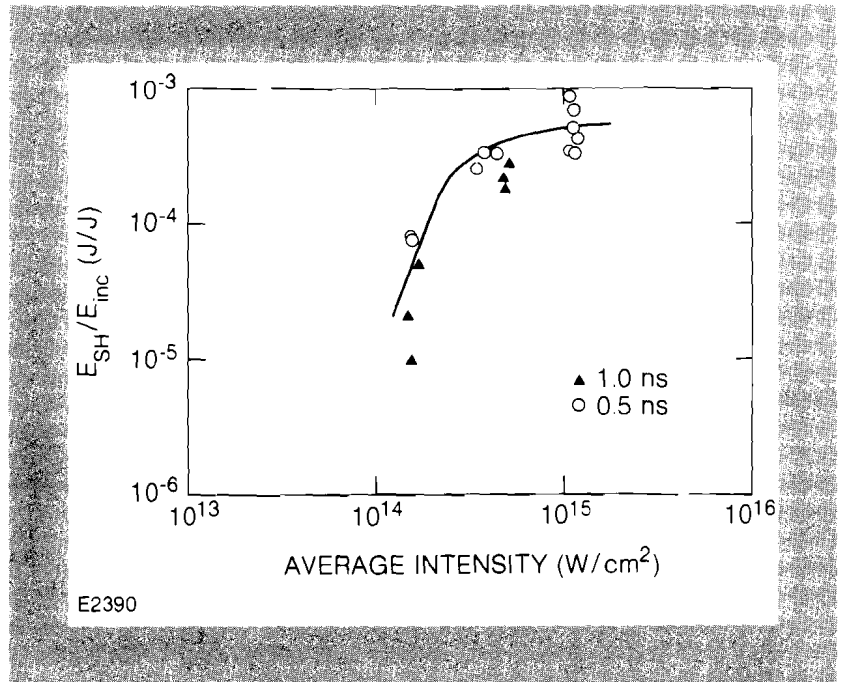


Fig. 22
Fraction of incident energy contained in the superhot electron distribution at 0.35 μm as inferred from the x-ray spectrum.

superhot electron energy and the $\omega_o/2$ emission, and because no increase in the x-ray signal is observed when the Raman instability occurs, we conclude that the superhot electron distribution is produced primarily by the $2\omega_o$ instability. The energy in the superhot distribution at saturation is small, less than 0.1% of the incident laser energy.

We performed a limited number of experiments at 1.05 μm on the GDL system by removing the frequency-conversion crystals. This permitted us to compare the continuum spectra at the two driver wavelengths using identical instrumentation. Two spectra obtained at comparable intensities, but at the two different wavelengths, are shown in Fig. 23. We find that the superhot component is present in both cases, but the hot component produced by resonance absorption is present only at 1.05 μm . Caution should be exercised, however, when comparing these spectra, on account of different target intensity distributions in the two cases and inadequate prepulse suppression in the IR experiments.

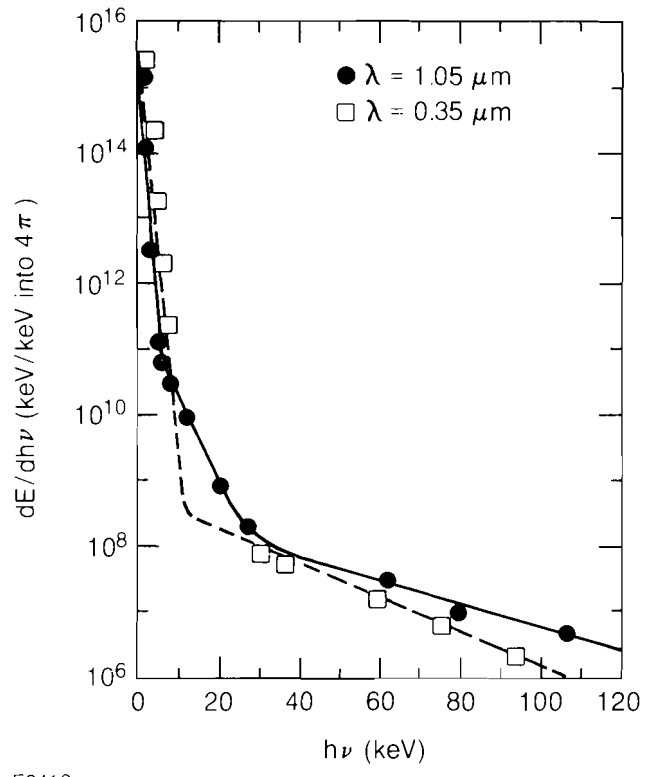


Fig. 23
Comparison of the spectra obtained with 1.05- μm (solid curve) and 0.35- μm (dashed curve) incident irradiation. Both spectra were obtained on the single-beam GDL facility.

Conclusion

The clear absence of any x-ray signature of resonance absorption in the 0.35- μm experiments, as well as the high measured absorptions and low preheat at 0.35 μm ,^{7,8} confirm that, as expected, the absorption of 0.35- μm laser light is dominated by inverse bremsstrahlung. Thus, the most persistent and detrimental source of hot electrons in

IR-laser-produced plasmas has been removed by going to shorter wavelengths. Another interesting feature of these measurements is the presence of a superhot-electron component at both laser wavelengths. Although this component accounts for less than 0.1% of the incident laser energy in these experiments, the extent to which superhot electrons are produced in the underdense corona will have to be monitored carefully as UV-laser-generated plasmas with larger scale lengths become available.

REFERENCES

1. A. B. Langdon, B. F. Lasinski, and W. L. Kruer, *Phys. Rev. Lett.* **43**, 133 (1979).
2. K. Estabrook, W. L. Kruer, and B. F. Lasinski, *Phys. Rev. Lett.* **45**, 1399 (1980).
3. K. Tanaka, L. M. Goldman, W. Seka, M. C. Richardson, J. M. Soures, and E. A. Williams, *Phys. Rev. Lett.* **48**, 1179 (1982). See also LLE Review 7, (1981).
4. K. Estabrook and W. L. Kruer, *Phys. Rev. Lett.* **40**, 42 (1978).
5. B. F. Lasinski, A. B. Langdon, K. G. Estabrook, and W. L. Kruer, Lawrence Livermore 1980 Annual Report UCRL-50021-80, p. 3-30 (1981).
6. K. A. Brueckner, *Nucl. Fusion* **17**, 1257 (1977).
7. W. Seka, R. S. Craxton, J. Delettrez, R. Keck, R. L. McCrory, D. Shvarts, J. M. Soures, and R. Boni, *Opt. Commun.* **40**, 437 (1982).
8. B. Yaakobi, J. Delettrez, L. M. Goldman, R. L. McCrory, W. Seka, and J. M. Soures, *Opt. Commun.* **41**, 355 (1982).

Section 3

TECHNOLOGICAL DEVELOPMENTS

3.A Monolithic Cell for Frequency Conversion

The origination¹ at LLE of the “polarization-mismatch” scheme for highly efficient energy conversion of Nd:glass laser radiation to its third harmonic ($3\omega = 351$ nm), and the subsequent demonstration of the process using two bare crystals of type-II KDP,² have provided the inertial-fusion program with an attractive approach towards improving the performance of laser-fusion targets. An overall energy-conversion efficiency of 80%, from 1ω ($\lambda = 1054$ nm) to 3ω ($\lambda = 351$ nm), was predicted and demonstrated for Nd:glass systems using real-beam temporal and spatial intensity profiles. The actual deliverable 3ω energy, however, has fallen below 80% because of problems with optical materials. Nonlinear loss processes at the second harmonic ($\lambda = 527$ nm)³ and photochemically induced degradation at the third harmonic⁴ have impeded the use of index-matching liquids for the recovery of energy losses from Fresnel reflections at the conversion-crystal surfaces.

An elegant conversion-cell design, which makes use of the polarization-mismatch tripling scheme, was developed by Summers *et al.* at Livermore.⁵ Two type-II KDP crystals are sandwiched in “tandem” in a single “monolithic” cell, separated from each other and from the cell windows by thin layers of index-matching fluid used to eliminate reflections from all internal surfaces.

We have adapted this design for use on our laser systems. A prototype cell has been successfully tested in our UV damage-testing

facility,^{6,7} and larger-aperture cells of the same design will be used for the conversion of the first six beams of OMEGA to 3ω in 1983. We have devoted considerable attention to long-term performance. We have tested a number of index-matching liquids and have selected Koolase,⁸ which we have found to perform well over several months of operation (over 400 shots); in particular, it exhibits good photo-chemical stability. Our design has also shown excellent alignment stability.

Monolithic-Cell Design

The polarization-mismatch concept for frequency conversion is shown schematically in Fig. 24. Both the KDP second-harmonic generator (SHG) and the KDP third-harmonic generator (THG) are type-II-cut, such that the z-crystallographic axis (the crystal optic axis) makes an angle of approximately 59° with the polished optical surface normal of each crystal. Laser radiation at 1ω , incident on the SHG, is linearly polarized at 35° to the o-direction of the doubler. Provided that the intensity of the incident laser radiation and the thickness of the SHG are appropriately matched,^{1,2} equal numbers of 1ω and 2ω photons emerge from the SHG, which is angle-tuned for phase matching. These photons are subsequently mixed in the THG to produce 3ω radiation. As indicated in Fig. 24, the THG is rotated with respect to the SHG by 90° about the system optical axis, and must therefore be angle-tuned in a plane orthogonal to that used to tune the SHG. Both crystals are of the same thickness in order to ensure optimum performance.⁹ The orthogonality of the SHG and THG crystals permits the design of a single frequency-conversion cell containing both crystals.

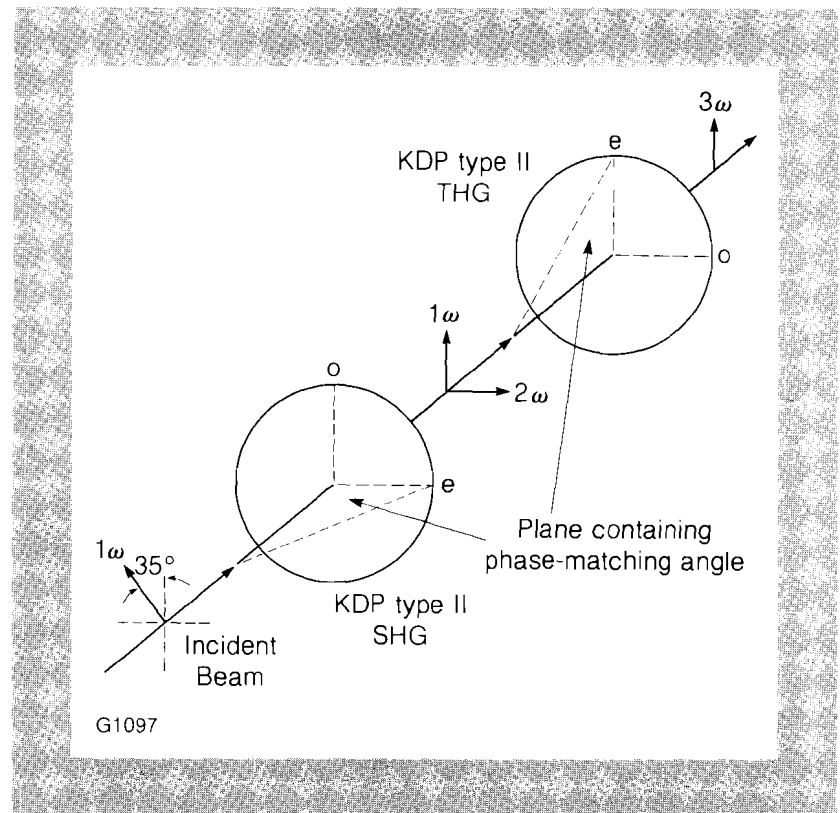


Fig. 24
Polarization-mismatch frequency conversion scheme. The incident 1ω radiation is polarized at 35° to the o-direction of the SHG to ensure that equal numbers of 1ω and 2ω photons emerge from the doubling stage. Both crystals are tuned about their o-directions to achieve phase-matching.

Angle tuning for proper phase matching is then accomplished in a standard gimbal mount.

Fig. 25
 Monolithic frequency-conversion cell. The SHG and THG crystals are held between a common pair of AR-coated, fused-silica end windows. "Koolase" index-matching liquid eliminates the six internal reflections of the cell, and all materials have been chosen for their chemical compatibility with this liquid. Liquid-layer thicknesses are maintained at 150 μm by glass spacers.

The design shown in Fig. 25 incorporates the SHG and THG crystals between a common pair of fused-silica windows. These four optical elements are gently, but firmly, held together by spring-loaded plungers and swivel pads. Three sets of glass spacers separate the crystals from each other and from the end windows, and enable index-matching liquid to coat all six internal optical surfaces. The two external surfaces of the cell possess dual-wavelength, 1ω and 3ω , AR coatings. The characteristics of materials chosen for the construction and testing of a 60-mm-clear-aperture device are indicated by the code in

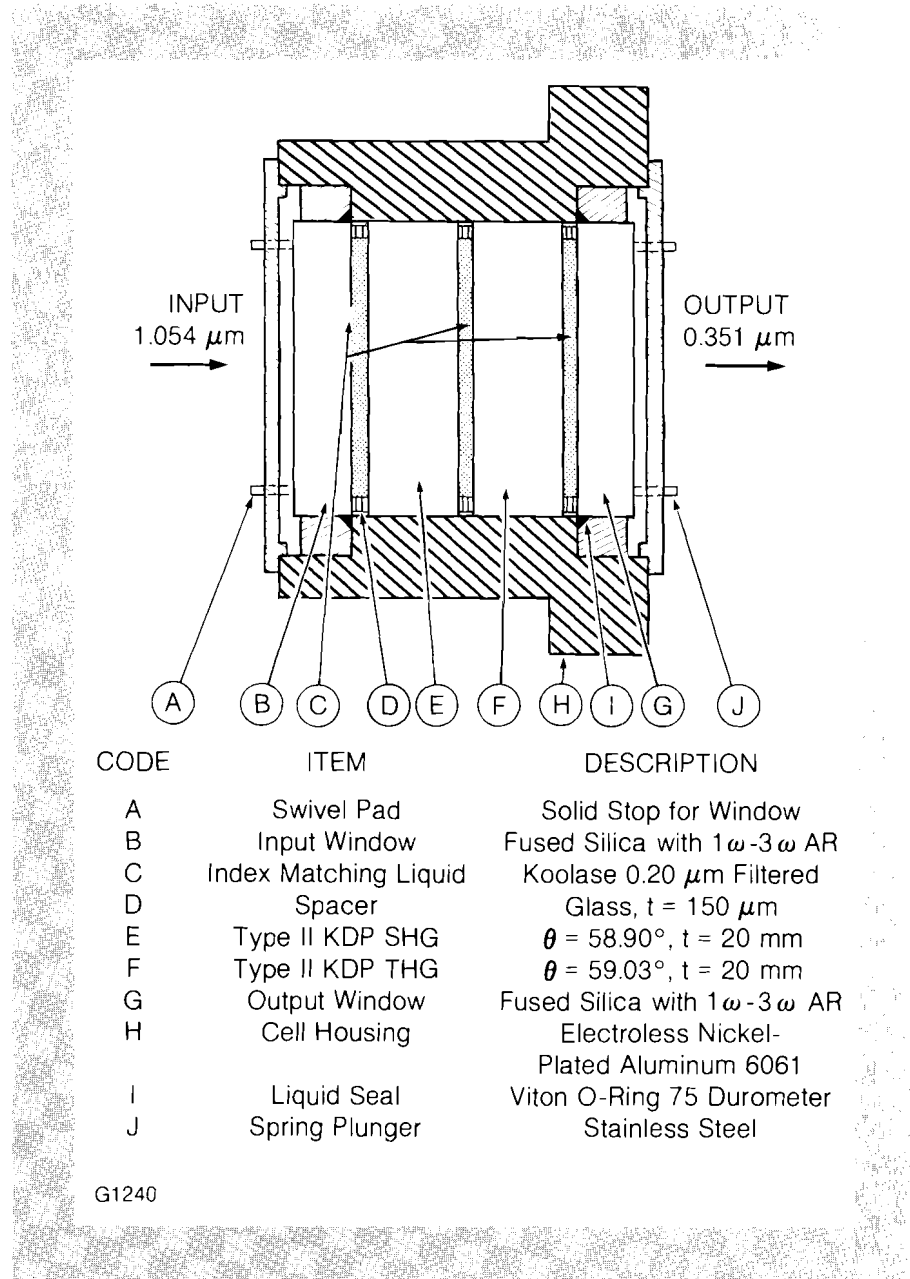


Fig. 25. The gimbal-mounted device is shown in Fig. 26. A thermistor temperature sensor, mounted within the cell body in close proximity to the crystals, controls current to an infrared heat lamp, which stabilizes the cell temperature to $\pm 0.05^\circ\text{C}$. Temperature stabilization is required to decouple the cell from temperature fluctuations that occur in the laser bay.

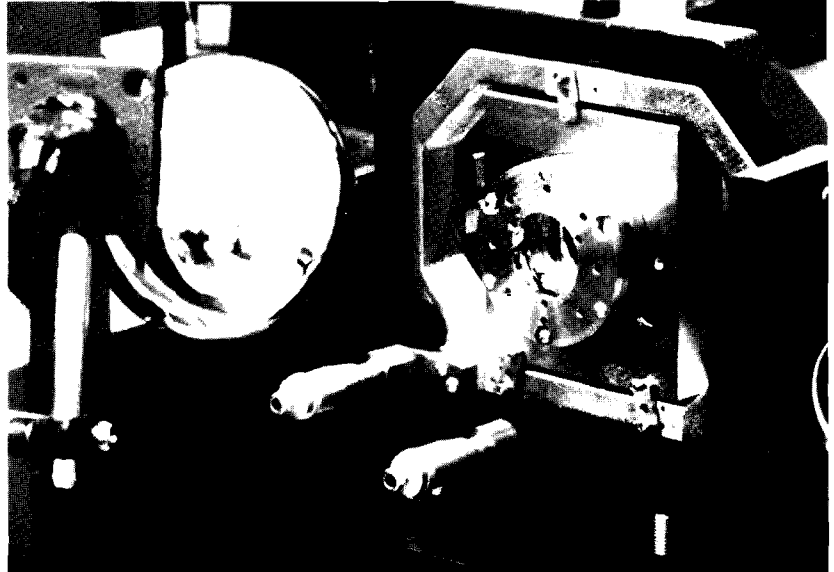


Fig. 26
60-mm-clear-aperture monolithic cell in a gimbal mount. The infrared heat lamp, visible in the foreground, stabilizes the temperature of the cell to 22°C . The cell is rotated about the vertical axis for doubler alignment and the horizontal axis for tripler alignment.

G1181

One obvious advantage of the monolithic-cell design, when compared with separate SHG and THG designs, is that it requires fewer optical elements and AR-coated surfaces. In addition, we have chosen to make the input and output windows identical to simplify spare-parts inventory. It is also convenient to use a single liquid for index matching of all internal surfaces.

Assembly and Testing

It is fundamental to the monolithic-cell configuration that the SHG and THG crystals be installed with their ordinary (o) and extraordinary (e) directions orthogonal, and that the o- and e-directions be distinguished from each other (see Fig. 24). Satisfying the former condition ensures that angle tuning one crystal in the gimbal mount is decoupled from angle tuning the second crystal. Satisfying the latter condition ensures that the SHG may be properly oriented with respect to the incoming 1ω laser radiation.

By utilizing the uniaxial birefringence of KDP, it is possible to devise a simple, inexpensive method for orienting and marking SHG and THG crystals prior to loading and filling the monolithic cell. Figure 27 demonstrates the two procedures required. Rotation of a crystal through 360° around its optical surface normal, while between crossed polarizers, produces four intensity minima in the lock-in-detected HeNe signal. These minima define the ordinary-ray and extraordinary-ray directions projected onto the polished crystal surface. These directions may be marked onto the crystal barrel. By orienting one of these directions at 45° to the incident HeNe polarization direction, the intensity between crossed polarizers can then be

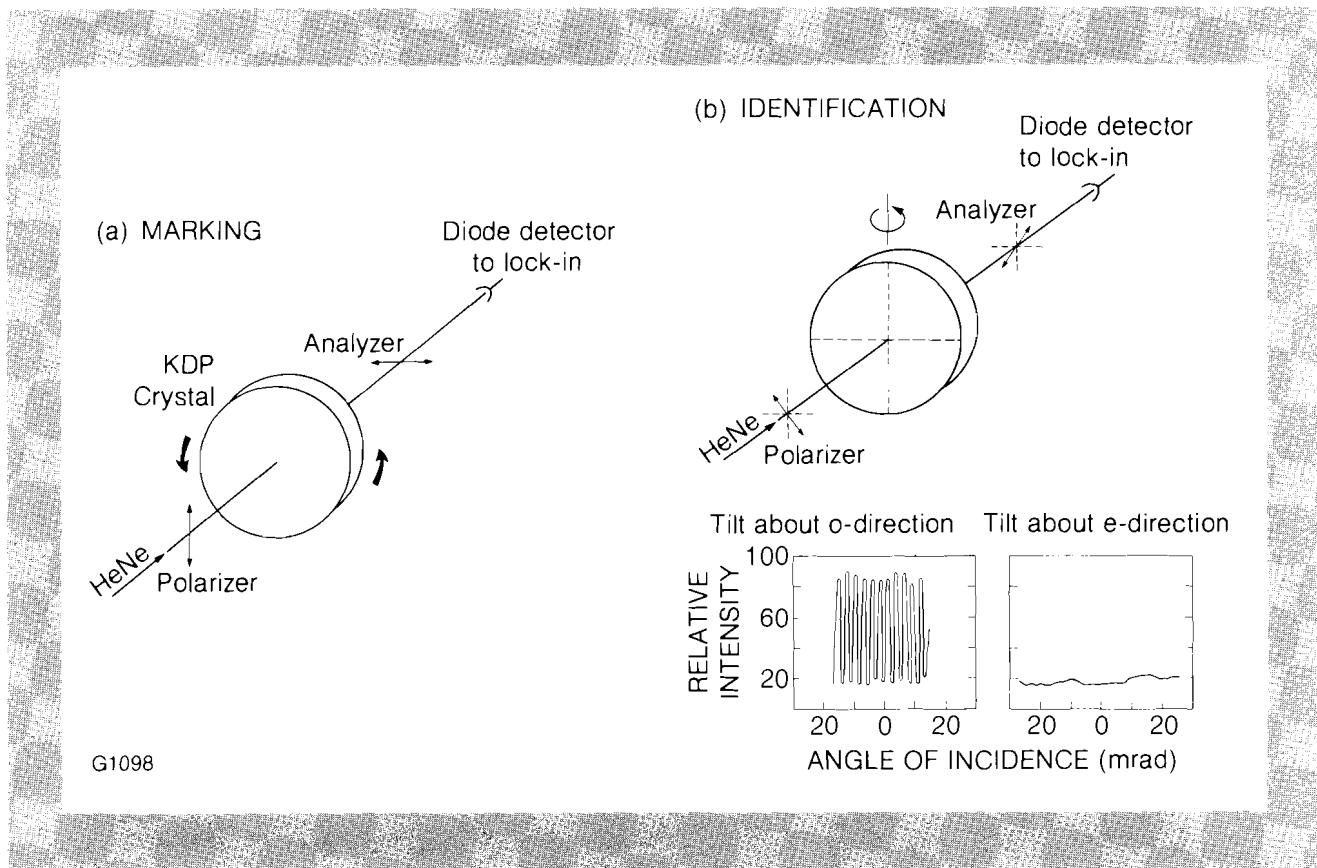


Fig. 27

a) Marking of the *o*- and *e*-directions is accomplished by rotating the KDP crystal 360° about its center while situated in a HeNe laser beam between crossed polarizers. The desired directions correspond to the four intensity minima observed.

b) The *o*- and *e*-directions are distinguished from each other by tilting the crystal about an axis of rotation coinciding with a set of barrel marks. A rapidly varying series of intensity maxima and minima result if the crystal is being tilted about its *o*-direction.

measured as a function of angle of incidence. If the axis of tilt and the *o*-direction coincide, a rapidly varying series of intensity maxima and minima, separated by about 1 mrad (depending on the crystal thickness), can be observed; this occurs because the angle between the propagation direction and the crystal optic axis is varied. (The actual values of the maxima and minima do not reach 100% and 0% in Fig. 27 because of the divergence of the HeNe laser beam.) If the axis of tilt and the *e*-direction coincide, very little intensity change over tens of mrad is observed. Both conditions are depicted in Fig. 27. This orientation technique can define the *o*- and *e*-directions of an SHG or THG crystal to within 60 seconds of arc, and is presently more sensitive than our ability to mark and mechanically orient circular crystals in a cell.

The 60-mm-clear-aperture monolithic conversion cell, shown in Fig. 26, has been operating in our UV thin-film, damage-testing facility^{6,7} since July 1982. Compared with the separate SHG/THG, two-cell method used prior to this date, the monolithic cell exhibits greatly improved long-term pointing stability and has generated a cleaner 3 ω beam.

Index-Matching Liquid

Koolase is the refractive index-matching liquid chosen for our monolithic conversion cell. This proprietary azeotrope is composed of esters, heterocyclic, and primary hydroxyl compounds.⁸ It has a viscosity of 2 cst. at 21°C, a refractive index of 1.44 at $\lambda = 337 \text{ nm}$,⁴

and negligible optical absorption at $\lambda = 527$ nm and $\lambda = 1054$ nm. The linear absorption coefficient for Koolase at $\lambda = 351$ nm can be as small as 0.37 cm^{-1} , but this may vary depending on the batch. This fluid was developed as a non-toxic, non-hygroscopic, laser-flash-tube coolant, and is therefore photochemically stable under intense UV irradiation. We have determined that Koolase is compatible with KDP and a number of other materials. Table 1 gives the results of a thirteen-month passive soak test, conducted at room temperature. Particulates may be removed from the $2.0\text{-}\mu\text{m}$ -filtered, as-purchased liquid, by additional filtering through a Nalge $0.20\text{-}\mu\text{m}$ nylon-membrane filter using a glass syringe.

Table 1
Compatibility of various materials with
Koolase.

<u>COMPATIBLE</u>	<u>NOT COMPATIBLE</u>	<u>WHY</u>
• KDP	• Transparent mylar	Swelling
• Fused silica	• Dyed mylar	Bleeding
• Indium	• Vinyl tubing	Increased UV absorption
• Gold	• Tygon tubing	Increased UV absorption
• 6061 Aluminum	• Gum rubber tubing	Increased UV absorption
• Black anodized aluminum	• Polyflo tubing	Increased UV absorption
• 316 stainless steel	• Silicon tubing	Increased UV absorption
• Polypropylene	• Buna N O-ring	Increased UV absorption
• Nylon membrane filter	• Neoprene O-ring	Bleeding
• Viton	• Polyurethane O-ring	Increased UV absorption
• Red silicon O-ring	• Black delrin	Increased UV absorption
• White silicon O-ring	• Lexan	Increased UV absorption
• White delrin	• Teflon TFE	Increased UV absorption
• Teflon PFA	• Copper	Chemical reaction
• Teflon FEP		
• RTV 108		

G1101

In both the 60-mm-aperture monolithic cell and a separate 140-mm THG cell installed on the GDL facility, Koolase has shown no long-term photochemically induced degradation to itself or to the KDP crystal surface over the past three to six months. During this time period, 350 laser shots were taken at an average 3ω fluence of 0.2 J/cm^2 , and 100 shots at 0.5 J/cm^2 , all with a pulse width of 1 ns. The passive absorption losses for 1ω , 2ω , and 3ω laser radiation in the three $150\text{-}\mu\text{m}$ -thick fluid gaps of the monolithic cell have remained below 1% total during this time period.

Halocarbon oil,^{3,10} another index-matching fluid that has been found effective and stable in a 140-mm SHG cell at $\lambda = 527$ nm, has not exhibited adequate photochemical stability in a 140-mm THG cell. Figures 28a and 28b indicate that, after two months and 200 shots of 351-nm radiation at 0.5 J/cm^2 , Halocarbon oil degraded within the cell and caused chemically induced etching of the polished KDP crystal surface.

Summary

We have described the design, construction, and performance of a monolithic cell for frequency conversion of moderate-intensity, Nd:glass laser radiation from $\lambda = 1054$ nm to $\lambda = 351$ nm. This design

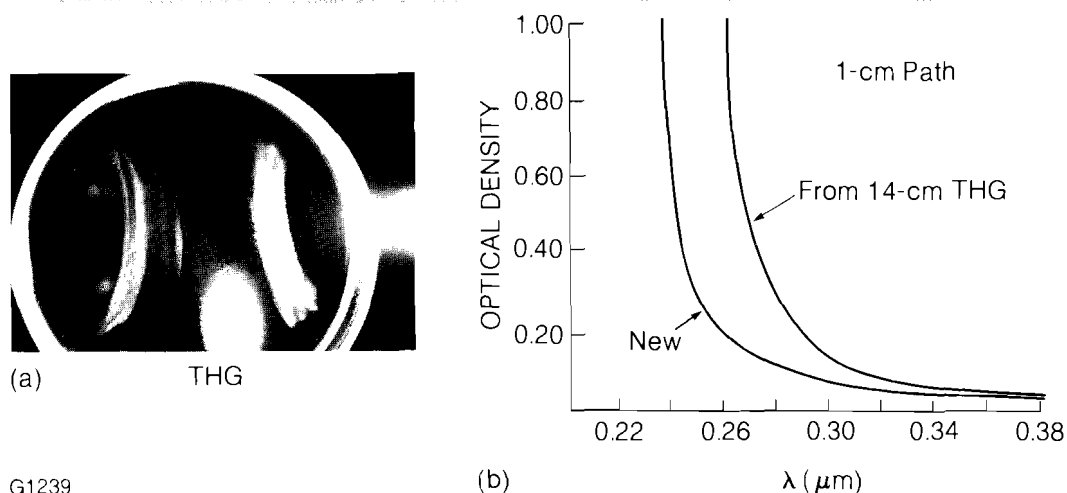


Fig. 28
 Incompatibility of Halocarbon oil with KDP in the presence of 3ω laser radiation. Photochemically induced degradation to Halocarbon oil after 2 months and 200 shots of 3ω radiation at 0.5 J/cm^2 resulted in chemical attack to a 140-mm THG-cell output surface. Optical scatter off the roughened and etched surface is evident in (a). A spectral scan comparing new and used oil [see (b)] shows that this liquid lacks chemical stability in the presence of 3ω laser radiation.

takes advantage of the highly energy-efficient polarization-mismatch conversion scheme, wherein two type II KDP crystals of equal thickness are orthogonally oriented between a common pair of cell windows. Long-term pointing stability and 3ω beam quality are enhanced with the monolithic-cell design. Long-term photochemical stability problems, associated with the use of index-matching liquid, have been solved by the choice of Koolase.

REFERENCES

1. R. S. Craxton, *Opt. Commun.* **34**, 474 (1980).
2. W. Seka, S. D. Jacobs, J. E. Rizzo, R. Boni, and R. S. Craxton, *Opt. Commun.* **34**, 469 (1980).
3. W. L. Smith, *Technical Digest - CLEO'81, OSA*, p. 32 (June 1981).
4. S. D. Jacobs and J. A. Abate, *Technical Digest - CLEO'81, OSA*, p. 86 (June 1981).
5. M. A. Summers, R. D. Boyd, D. Eimerl, and E. M. Booth, *Technical Digest - CLEO'81, OSA*, p. 30 (June 1981); M. A. Summers, L. G. Seppala, F. Rienecker, D. Eimerl, and B. C. Johnson, "Engineering Design of the Nova Laser Facility for Inertial Confinement Fusion" by W. W. Simmons *et al.*, Chap. 8, LLNL Report CONF-811040 (1982).
6. J. A. Abate, *Technical Digest - CLEO'81, OSA*, p. 86 (June 1981).
7. J. A. Abate, R. Roides, S. D. Jacobs, W. Piskorowski, and T. Chipp, 14th Annual Symposium on Optical Materials for High-Power Lasers, Boulder, CO, November 1982.
8. Available from Kimball Associates, 846-B Rummell Road, St. Cloud, FL 32769.
9. R. S. Craxton, *IEEE J. Quantum Electron.* **QE-17**, 1771 (1981).
10. Available from Halocarbon Products Corp., 82 Burlews Court, Hackensack, NJ 07601.

3.B Rotational-Shearing Interferometry for Improved Target Characterization

Inertial-fusion targets have strict requirements regarding sphericity, surface smoothness, and layer-thickness uniformity. During fabrication, each target must be fully characterized to allow for the interpretation of experimental target shot data. We report here a new interferometric technique for the characterization of transparent targets.

Interferometric characterization techniques have been extensively used to measure target quality. An imperfect target, which can be described as a superposition of defects on a perfect spherical shell, produces an interferogram with the defect and perfect-shell components combined. It is often difficult to separate the defect-produced components in a target interferogram from the concentric fringe pattern produced by a perfect target; this limits precise interpretation of the target defects. We have used the rotational symmetry of a perfect target to improve defect-detection sensitivity by using rotational-shearing interferometry. One advantage of this approach is that rotationally symmetric objects produce null interferograms, making only the non-rotationally symmetric defects visible. Another advantage is that shell nonconcentricity can be measured independently of shell thickness. We have developed a simple analytical model which describes the interferometer's operation, and have constructed and tested a prototype device for fusion-target characterization.

Characterization of optically transparent target shells has generally been performed with interferometry.¹ The interferometers used have been primarily of the Twyman-Green,² Mach-Zehnder,³ or lateral-shearing⁴ configurations. Common to the operation of each of these instruments is the superposition and interference of the wave front passing through the target with a uniform plane wave front. The resultant interference pattern produced by a perfect target is a "bull's-eye" pattern rotationally symmetric about the target center. A non-axially symmetric target defect produces an asymmetry in the interference pattern, and measurement of this asymmetry has been the basis for characterizing the wall-thickness uniformity of targets. This approach has limitations because the defect-detection sensitivity is inversely proportional to target-shell thickness.⁵ Thick target shells require a larger defect size for detectability.

The axial symmetry of inertial-fusion targets suggests the use of another interferometric characterization method, rotational-shearing interferometry. Here the wave front is passed through the target and then split into two parts; one part is rotated through an angle θ , and the two wave fronts are then recombined causing interference.⁶ This technique has several advantages over conventional interferometry for fusion-target characterization. The detection sensitivity of shell-thickness nonuniformity has a fixed value. Also, the background bull's-eye pattern is not present, which makes local defects easier to detect. The most significant advantage of rotational-shearing interferometry is that it is an easily analyzed null test. A perfect fusion

target produces a uniform flat field, i.e., no fringe pattern is produced.

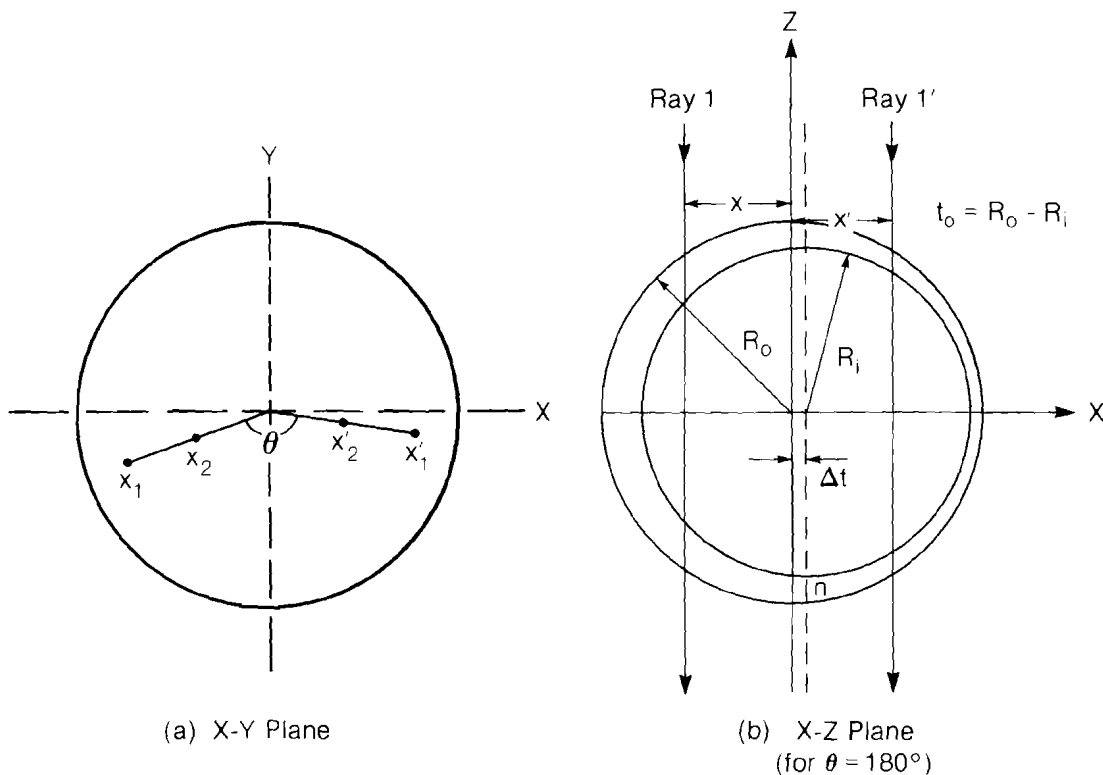
Various other types of interferometry have been developed that are also null tests. These have included flip-image,⁷ 90° views,⁷ and holographic⁸ systems. Although these are usable as null tests, the interferograms produced are difficult to analyze.

Concept of Rotational-Shearing Interferometry

Rotational shearing superimposes a ray parallel to the z axis that intersects the target at (x,y) with a parallel ray passing through (x', y') (Fig. 29a). The relationship between these superimposed rays is given by a rotation about the z axis through an angle θ .

An x-z plane cut through a nonconcentric spherical shell having the defect axis aligned along the x axis is shown in Fig. 29b. The nonconcentricity Δt of the shell, defined as the distance separating the centers of the inner and outer spherical surfaces, can be obtained directly from rotational-shearing measurements. Neglecting refraction, a ray in the x-z plane passing through x, from $z = R_o$ to $z = -R_o$, has an optical path length (OPL) of:

Fig. 29
Configuration for rotational-shearing interferometry. A laser beam is passed through the glass shell parallel to the z axis, and is then split into two beams which are rotated through a relative angle of θ before being recombined to produce an interferogram. Rays intersecting the shell at x_1 and x'_1 will interfere with each other, as will rays at x_2 and x'_2 . The nonconcentricity may be determined by counting fringes between adjacent points x_1 and x_2 .



T634

T567

$$\text{OPL}(x) = 2(n-1) \left\{ (R_o^2 - x^2)^{1/2} - [(R_o - t_o)^2 - (x - \Delta t)^2]^{1/2} \right\} + 2R_o \quad (1)$$

where n is the refractive index of the shell, R_o is the outer radius of the shell, t_o is the average shell thickness, and the refractive index interior and exterior to the shell is 1.0. Refraction is ignored here; a more detailed analysis shows that this omission does not lead to significant errors for small values of Δt .

Consider a second ray from the rotated image passing through (x', y') that is superimposed on the nonrotated ray. For the case $\theta = 180^\circ$, $x' = -x$, and the difference in optical paths between the two nonrefracting rays, to first order in R_o^{-1} , is given by:

$$\text{OPD}(x) = \text{OPL}(x) - \text{OPL}(-x) = 2(n-1) \left(-\frac{2x\Delta t}{R_o} \right), \quad (2)$$

where it is assumed that

$$\frac{t_o}{R_o} \ll 1 \text{ and } \frac{x^2}{R_o^2} \ll 1.$$

The number of interference fringes produced between $(x_1, 0)$ and $(x_2, 0)$ is

$$m \equiv \left| \frac{\text{OPD}(x_1) - \text{OPD}(x_2)}{\lambda} \right| = \frac{4(n-1)}{\lambda} |x_1 - x_2| \frac{\Delta t}{R_o} \quad (3)$$

where λ is the wavelength of the light. Equation (3) can be inverted to give the noncentricity Δt directly from the number of fringes.

Lateral shear, introduced through misalignment of the target shell from the rotational axis of the interferometer, has been analyzed and found not to affect the noncentricity measurement to first order. Also, the shell thickness t_o does not appear in Eq. (3). This is in contrast with previous interferometric characterization techniques where $\Delta t \propto 1/t_o$.⁵

Orientation of the noncentricity defect in the x - y plane gives the greatest defect-detection sensitivity. Rotation of the defect axis away from the plane by an angle Φ decreases sensitivity to Δt by a factor of $\cos \Phi$.² In practice, the target shell can be oriented with $|\Phi| \leq 10^\circ$, causing a decrease in sensitivity which is less than 3%.

Equation (3) expresses the relationship between shell noncentricity and interference measurements produced with 180° of rotational shear. Having the rotational-shear angle θ different from 180° reduces the noncentricity defect-detection sensitivity by $1 + \cos \theta$, which is small for θ near 180° . Aligning the rotation angle to within 10° of 180° presents no difficulties and reduces detection sensitivity by less than 3%.

Interferometer

Based on the encouraging results of the analytical model, an experimental apparatus was constructed. Figure 30 is a schematic of the instrument. The assembled interferometer, of the Mach-Zehnder configuration, uses matched components in each arm. The optical components were chosen so that only rotationally symmetric (spherical) aberration is introduced into each of the two beams. The aberrations are equal and cancel when the beams recombine. Plate beam splitters and dove prisms, which introduce astigmatism in a diverging wave front, were not used. Instead, beam splitting and rotation were performed with cube beam splitters and mirror-image rotators. Figure 31 is a photograph of the experimental rotational-shearing interferometer.

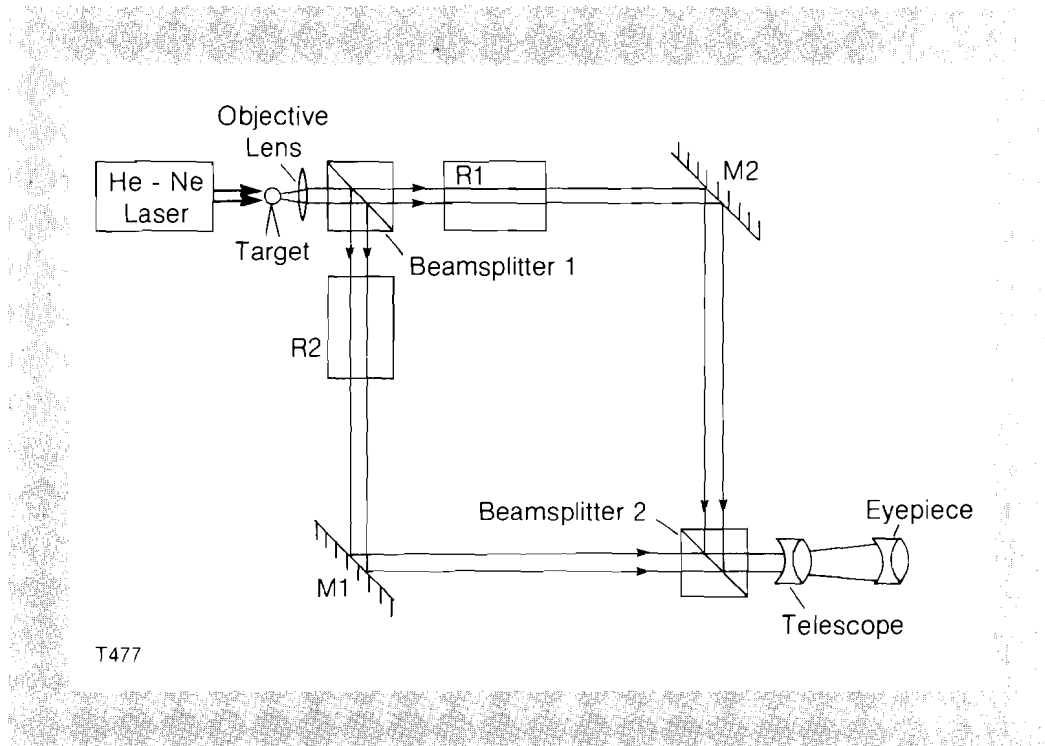


Fig. 30
Schematic of rotational-shearing interferometer.

The microscope objectives are corrected for use at infinite conjugates to ensure a minimum of image degradation from the long effective tube length of the microscope. A telescope assembly used at the interferometer's output cube beam splitter relays the image to the eyepiece.

The interferometer has approximately a half-wavelength of phase noise across its aperture. This arises primarily from defects in the cube beam splitters. Since this phase noise makes interpretation of small defects in targets difficult, two solutions were investigated to eliminate this problem. One involved using higher-quality optics in the interferometer, and the other involved operating the interferometer in an ac-phase-measurement mode. In the first case, the problem is minimized by reducing phase noise. In the second case, the noise is measured separately from the target and subtracted from the target measurement; this is the more desirable solution.

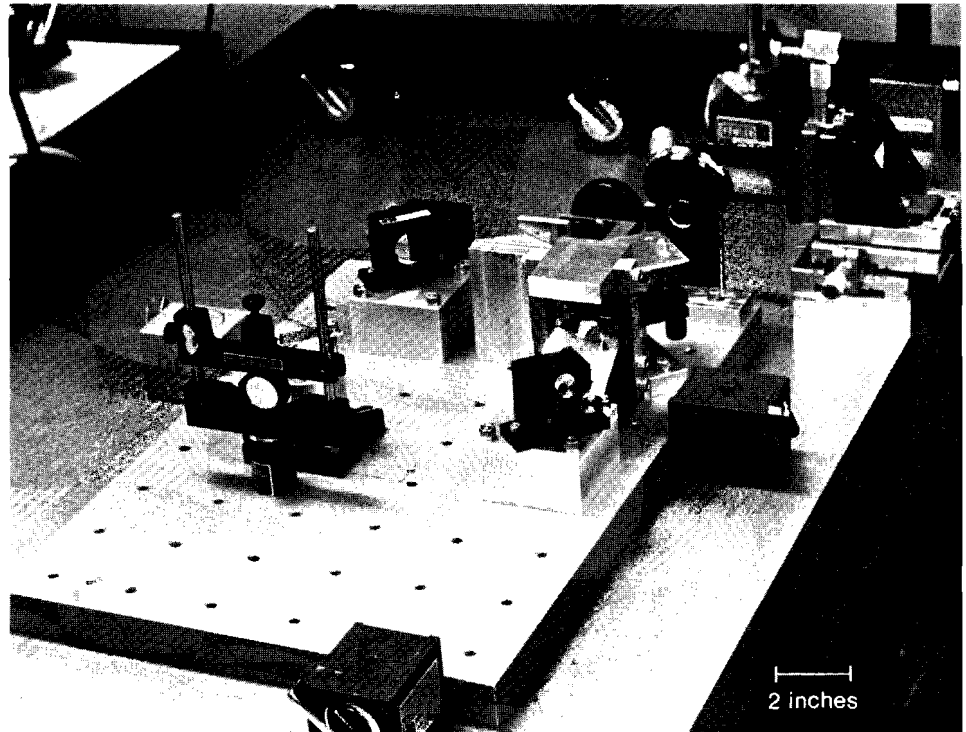


Fig. 31
The rotational-shearing interferometric apparatus with objective lens at upper right.

T563

Target-Shell Measurements

Targets are placed at the focal plane of the microscope's objective lens for characterization. The targets, supported either by a capillary stalk or by a microscope slide, are held by a precision micro-manipulator having micrometer positioning capability. The two images from the interferometer are superimposed by moving the target to the rotation axis of the interferometer. Target images can be visually superimposed to $\pm 1\%$ of their diameter.

The interferogram shown in Fig. 32a was produced by a target ($350\ \mu\text{m}$ in diameter, $3.4\text{-}\mu\text{m}$ shell thickness) that was displaced from the axis of rotation by a distance greater than its radius. With this degree of misalignment, the instrument operates like a lateral-shearing interferometer and produces two bull's-eye images similar to those from conventional interferometry.²

The interferogram in Fig. 32b was obtained from the same target, but using the rotational-shearing interferometer with less than $R_0/50$ misalignment of the two superimposed images. Here, parallel fringes perpendicular to the defect axis are evident. These can be used in Eq. (3) to quantify the degree of target-shell nonconcentricity. The measured fringe separation ($m=1$) in Fig. 32b produced by $0.6328\text{-}\mu\text{m}$ light is $113\ \mu\text{m}$. The nonconcentricity calculated using Eq. (3) is $\Delta t = 0.5 \pm 0.05\ \mu\text{m}$. This result was checked using the method of fringe-pattern decentration on Fig. 32a and found to agree to within 5%.⁵

Interferograms of a second target shell are shown in Figs. 32c and 32d. In Fig. 32c, the shell is displaced in the interferometer as in Fig.

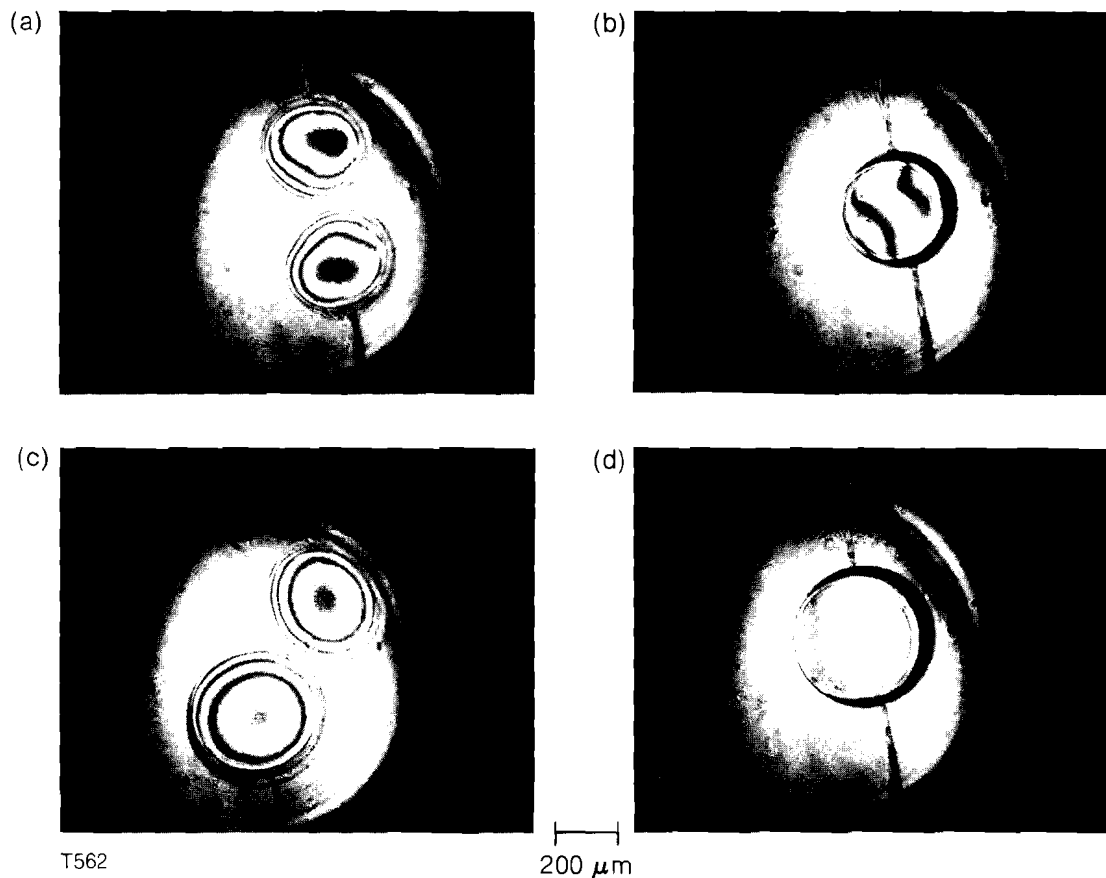


Fig. 32
 Conventional total-shearing interferograms (left) and rotational-shearing interferograms (right) of two stalk-mounted glass microballoons (top: 350- μm diameter; bottom: 425- μm diameter; both 3.4 μm thick). The rotational-shearing interferograms indicate nonconcentricities of 15% and <2% respectively.

32a, while in Fig. 32d, the images are superimposed with a minimum of lateral shear as in Fig. 32b. Figure 32d shows that this target has no detectable nonconcentricity defect; no detailed analysis is needed to interpret this interferogram. In contrast, it would be difficult to interpret the bull's-eye interference pattern of Fig. 32c.

Summary

A rotational-shearing interferometer offers distinct advantages for characterizing transparent inertial-fusion targets. The sensitivity of the instrument to nonconcentricity defects is independent of target-shell thickness, resulting in improved concentricity characterization of thick-walled targets. Since the device is inherently a null-test instrument, defects not easily visible using conventional target-characterization techniques can be readily recognized. This results because highly concentric shells do not produce the usual bull's-eye interference pattern. This apparatus appears to be well suited to analyzing fuel-layer uniformity in transparent cryogenic targets.

Additional work is needed to improve the performance of the instrument. The incorporation of wave-front-measuring techniques such as

ac interferometry would add to the sensitivity of the instrument and relax the quality requirements of the optical components. Another potential improvement involves varying the rotational-shearing angle θ . This would enable the instrument to locate and measure defects other than nonconcentricity.

REFERENCES

1. B. W. Weinstein, *J. Vac. Sci. Technol.* **20**, 1349 (1982).
2. R. R. Stone, D. W. Gregg, and P. C. Souers, *J. Appl. Phys.* **46**, 2693 (1975).
3. P. O. McLaughlin and D. T. Moore, *J. Opt. Soc. Am.* **67**, 1386 (1977).
4. J. R. Miller and J. E. Sollid, *Appl. Opt.* **17**, 852 (1978).
5. T. F. Powers, *J. Vac. Sci. Technol.* **20**, 1355 (1982).
6. M. V. R. K. Murty and E. C. Hagerott, *Appl. Opt.* **5**, 615 (1966).
7. B. W. Weinstein, H. Medeck, J. A. Monjes, R.M. Singleton, and D.L. Willenborg, Lawrence Livermore 1978 Annual Report, UCRL-50021-78, 4-31, 1979.
8. T. P. Bernat, D. H. Darling, and J. J. Sanchez, *J. Vac. Sci. Technol.* **20**, 1362 (1982).

Section 4

BRIEF UPDATES

4.A Progress Toward Terahertz Electronics

In a recent issue of the LLE Review¹, a novel technique for time-resolving electrical signals with subpicosecond resolution and μV sensitivity was reported. This technique is based on the inherently fast ($< 10^{-15}\text{s}$) Pockels effect induced in a traveling-wave electro-optic modulator by the signal under study. The signal-induced birefringence is probed with 100-fs optical pulses. When operated in a “velocity-matching” arrangement, a theoretical limit of 500 fs was achieved. This limit is due to the diameter of the optical-probe beam waist. In the previous result, shown in Fig. 33a (or Fig. 21c of Ref. 1), the signal generated by a photoconductive detector when triggered by a 100-fs optical pulse exhibits double-hump behavior. It was hypothesized that this waveform was a direct consequence of the relatively low TEM cutoff frequency of the traveling-wave modulator. The leading edge of the signal waveform was attributed to the “direct-wave” or TEM field, whereas the second hump was thought to be due to an additional TM wave propagating noncollinearly with the electrodes and consequently arriving at a later time at the sampling point. This time delay was found to be close to the delay calculated for the physical dimensions and effective dielectric constant of the transmission line.

To eliminate the TM wave, we raised the TEM cutoff frequency of the traveling-wave modulator by decreasing the substrate thickness from $250\ \mu\text{m}$ to $100\ \mu\text{m}$. The result is shown in Fig. 33b, where the signal exhibits only the TEM contribution. A small foot is displayed at the leading edge of the step function; this is attributed to electrical

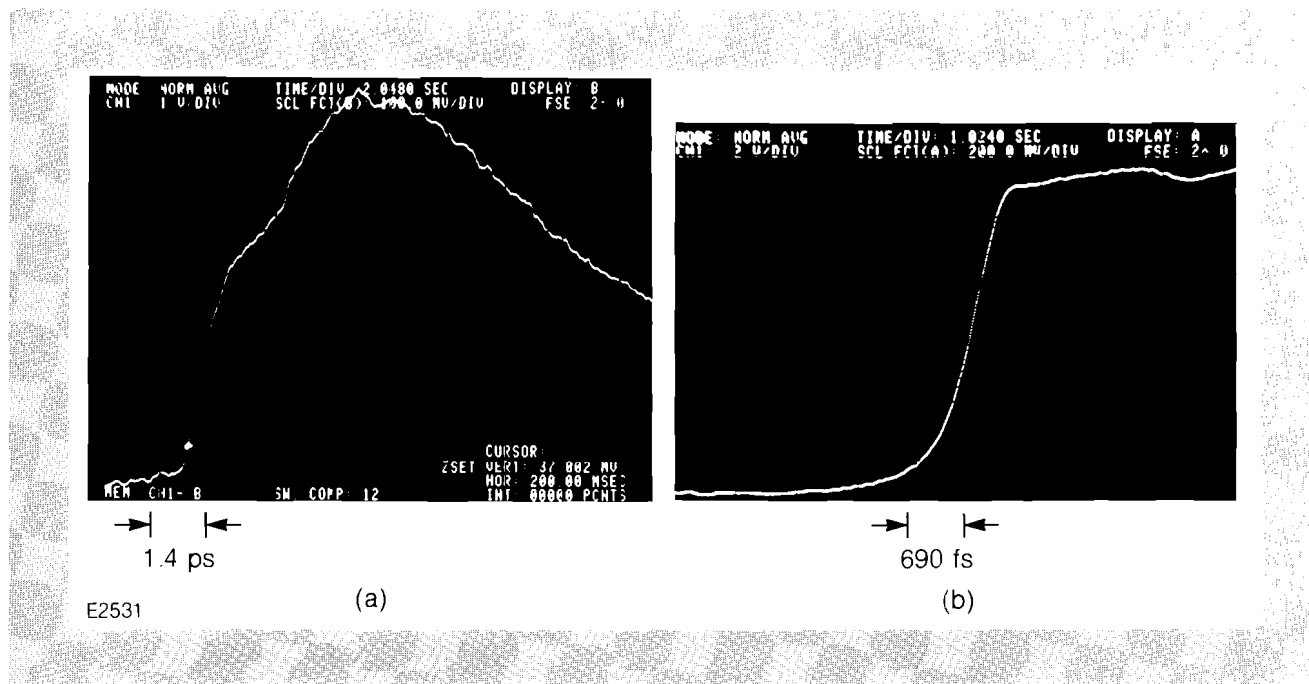


Fig. 33
Response of a Cr-doped GaAs photoconductive detector as measured by a 100-fs focused laser pulse with beam diameter less than 20 μm .

- a) 250- μm substrate
- b) 100- μm substrate

dispersion experienced by the signal as it propagates approximately 100 microns from the source to the sampling point. The fastest slope of the leading edge is indicative of an intrinsic sampling time of 500 fs (10%-90%).

This result shows that electronics with an unprecedented bandwidth of 1 THz can be achieved. It represents an improvement from one to two orders of magnitude over the state of the art in electrical sampling. Consequently, we expect this technique to have profound implications for the study of laser-semiconductor interactions in the propagation of electrical pulses and the characterization of ultra-fast electronic components.

REFERENCES

1. LLE Review 11, 22 (1982).

Section 5

NATIONAL LASER USERS FACILITY NEWS

This report covers the activities of the National Laser Users Facility (NLUF) during the quarter October to December 1982. During this period five users conducted experiments on LLE facilities. The visiting scientists associated with these experiments represented UCLA, Yale University, the Naval Research Laboratory, the University of Maryland, the University of Pennsylvania, the University of Connecticut, and the University of Rochester.

Five user experiments were conducted in this quarter, compiling a total of 120 shots on the Glass Development Laser (GDL) and the OMEGA laser system. Table 2 gives a summary of the number of shots for each user experiment.

Research scientists from the following institutions participated in the experiments:

1. Francis Chen, Chan Joshi, and Humberto Figueroa (UCLA), and Nizarali Ebrahim (Yale University).
2. J. Kent Blaise, D. Pierce, Donatella Pascolini, and A. Scarpa (University of Pennsylvania).
3. Leo Herbette and Robert McDaniel (University of Connecticut).
4. James Forsyth and Robert Frankel (University of Rochester).

User System Shot Distribution
October 1 to December 31, 1982

<u>USER</u> (Principal Investigator)	<u>FACILITY</u>	<u>NUMBER OF SHOTS</u>
UCLA/Yale University (F. Chen)	GDL	48
University of Pennsylvania (J. K. Blaise)	GDL	14
University of Connecticut (L. Herbette)*	GDL	--
University of Rochester (J. Forsyth)	GDL	44
Naval Research Laboratory (U. Feldman)	OMEGA	14
	TOTAL	120

*Shared shots with the University of Pennsylvania

U65

Table 2
User system shot distribution from October 1 to December 31, 1982.

5. Uri Feldman and George Doschek (Naval Research Laboratory), Samuel Goldsmith (University of Maryland), and W. E. Behring (Goddard Space Flight Center).

This issue of the LLE Review highlights results from the Naval Research Laboratory experiment entitled "Spectral Lines of High-Z Ions" (principal investigator, Uri Feldman).

A laser-produced plasma is a very efficient and interesting source for the study of spectral lines of highly ionized atoms. The high irradiation intensities and the spherically uniform illumination obtained with the OMEGA laser at LLE produce a very dense hot plasma ($N_e \sim 10^{21} - 10^{22} \text{ cm}^{-3}$, $T_e \sim 0.5 - 2 \text{ keV}$). In such plasmas high-Z atoms (where Z is the nuclear charge) lose most of their electrons and the resultant ions are strongly excited, emitting rich line spectra in the x-ray and extreme-vacuum-UV (XUV) spectral region (5-300 Å). The study of the XUV spectra emitted by the plasma ions is of great interest as a diagnostic tool, determining the physical characteristics and parameters of the plasma. Furthermore, XUV spectroscopy is significant for the advance of atomic physics (specifically, the study of the atomic structure of high-Z ions) and for the possible development of x-ray and soft-x-ray lasers.

The work described here was motivated by the last two goals. First, known spectra of some high-Z ions were obtained to examine the properties of the XUV spectra emitted from laser-produced plasmas. For this purpose the spectra of highly ionized Fe, Ni, Cu, and Mo were obtained and compared with data found in the literature. Second, the less-known spectra of highly ionized Ge, Kr, and Ta were recorded and some new atomic levels were identified. In the present study, a particular effort was made to observe and identify new transitions in Ne-like krypton (Kr^{25+}).

Hot, dense plasmas were produced by focusing the 24 laser beams of OMEGA onto spherical glass-microballoon targets of $\sim 1\text{-}\mu\text{m}$ thickness coated with layers of the elements to be studied. The microballoons usually contained no gas except when the spectra of gaseous elements were studied. Several spectra were also recorded from targets which were not prepared for our specific experiment, but for another study; in these cases, the targets generally had a complex multilayered structure. The diameter of a microballoon ranged from $200\ \mu\text{m}$ to $630\ \mu\text{m}$, the duration of the laser pulse was about 1 ns, and the total laser energy varied between 500 and 2400 J. The intensity of radiation on the target varied in the range of $1 \times 10^{14} - 5 \times 10^{15}\ \text{W/cm}^2$. Sometimes several shots, taken under relatively constant irradiation conditions, were integrated to obtain sufficient line intensity.

The spectra were observed with a 3-m grazing-incidence spectrograph at an incidence angle of 88° .¹ The grating was ruled with 1200 ℓ/mm , yielding a plate factor in the first order of $0.2\ \text{\AA}/\text{mm}$ at $16\ \text{\AA}$. In order to enhance the radiation flux to the grating, the radiation from the plasma was focused onto the spectrograph entrance slit using a cylindrical concave mirror. The mirror was fabricated from a Be strip, coated by high-Z elements and bent to obtain a grazing-incidence reflection of the XUV region. The design of the mirror is given in detail by Underwood.² The spectra were calibrated by means of known lines of oxygen, silicon, carbon, and some known lines of the observed elements. The wavelength calibration may be affected by the relative mass motion of the various ionic components of the plasma. Though it is difficult to estimate the errors at present, we believe that they are somewhat below $5\ \text{m}\text{\AA}$ for lines in the region of 10 to $90\ \text{\AA}$.

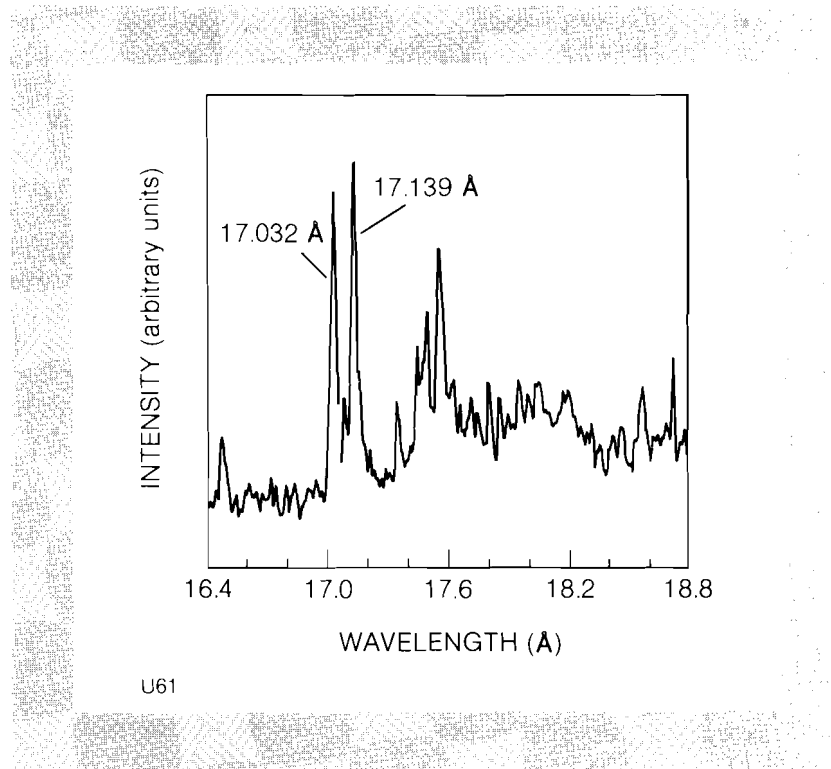


Fig. 34
Spectral lines of MoXXXII (Mo^{31+}) in the wavelength region of 17 to $18\ \text{\AA}$.

The spectra of eleven elements (C, N, O, Al, Si, Ni, Cu, Ge, Kr, Mo, and Ta) were obtained in the region of 10 to 95 Å. We were particularly interested in the spectra of highly ionized Ni, Cu, Kr, Ge, and Mo. In Fig. 34, the spectrum of highly ionized Mo is shown in the region of 17 to 18 Å; the stronger line in Fig. 34 corresponds to MoXXXII (Mo^{31+}), Na-like Mo. Other spectral transitions in Mo^{31+} , Mo^{30+} , and Mo^{29+} are shown in Table 3. In the Kr spectra, lines of Kr^{25+} were identified for the first time. These lines are presented in Table 4. Excellent agreement between theory³ and experiment was obtained. Some unidentified lines, which may be other Kr lines, are also listed in Table 4.

The observed spectra of most other elements (except for Ge and Ta) agree well with published data, but some noticeable irregularities in relative line intensities were observed in the spectra of Li-like Cu, Ni, and Si. The absence of some normally strong lines from these spectra is presently under study and an effort is being made to relate this observation to the physical properties of the plasma.

Table 3
Observed short-wavelength transitions in
MoXXX-XXXII ($\text{Mo}^{29+} - \text{Mo}^{31+}$).

<u>ION</u>	<u>CLASSIFICATION</u>	<u>J-J</u>	<u>λ (Å)</u>	<u>PREVIOUS MEASUREMENT^a</u>
MoXXXII	$3p^2P-4d^2D$	3/2-5/2	15.456	15.456
MoXXXII	$3p^2P-4d^2D$	3/2-3/2	15.505	15.504
MoXXX	$3p^2P-4d^2D$	1/2-3/2	15.630	15.627
			15.694	15.694
			15.755	15.756
			16.033	16.033
			16.273	
MoXXXII	$3p^2P-4s^2S$	1/2-1/2	16.481	16.480
MoXXXII	$3d^2D-4f^2F$	3/2-5/2	17.032	17.033
MoXXXII	$3p^2P-4s^2S$	3/2-1/2	17.088	17.086
MoXXXII	$3d^2D-4f^2F$	5/2-7/2	17.139	17.140
MoXXXII	$3d^2D-4f^2F$	5/2-5/2	17.161	17.165
			17.325	
MoXXX	$3p^2P-4s^2S$	1/2-1/2	17.355	17.355
MoXXXI	$3s3d^3D-3s4f^3F$	1-2	17.444	17.445
MoXXXI	$3s3d^3D-3s4f^3F$	2-3	17.493	17.500
MoXXXI	$3s3d^3D-3s4f^3F$	3-4	17.555	17.556
			17.812	17.815
MoXXXI	$3s3d^1D-3s4f^1F$	2-3	17.865	17.871
MoXXXII	$3d^2D-4p^2P$	5/2-3/2	18.573	18.573

a) P. G. Burkhalter, J. Reader, and R. D. Cowan, *J. Opt. Soc. Am.* 67, 1521 (1977).

TRANSITION	λ_{exp} (Å)	λ_{cal} (Å)
$3s^2S_{1/2} - 4p^2P_{3/2}^0$	21.181	21.183
$^2S_{1/2} - ^2P_{1/2}^0$	21.350	21.370
$3p^2P_{1/2} - 4d^2D_{3/2}$	22.255	22.256
$^2P_{3/2} - ^2D_{5/2}$	22.735	22.741
$3d^2D_{3/2} - 4f^2F_{5/2}$	25.605	25.618
$^2D_{5/2} - ^2F_{7/2}$	25.715	25.724
	22.195	
	23.877	
	37.762	
	37.859	
	37.926	

Table 4
Observed and calculated lines of Kr XXVI
(Kr⁺²⁵).

Further information on the NLUF is available by writing to:

Thomas C. Bristow, Manager
National Laser Users Facility
Laboratory for Laser Energetics
University of Rochester
250 East River Road
Rochester, New York 14623

REFERENCES

1. W. E. Behring, R. J. Ugiansky, and U. Feldman, *Appl. Opt.* **12**, 528 (1973).
2. J. H. Underwood, *Space Science Instrum.* **3**, 259 (1977).
3. L. L. Ivanov and E. P. Ivanova, *Atomic Data and Nuclear Data Tables* **24**, 95 (1979).

PUBLICATIONS AND CONFERENCE PRESENTATIONS

Publications

R. S. Marjoribanks, M. C. Richardson, J. Delettrez, S. Letzring, W. Seka, and D. M. Villeneuve, "Time-Resolved X-Ray Spectrometry of UV-Laser-Produced Plasmas," *Opt. Commun.* **44**, 113-116 (1982).

S. D. Jacobs, Y. Asahara, and T. Izumitani, "Optical Glass Wave Plates," *Appl. Opt.* **21**, 4526-4532 (1982).

R. W. Short, R. Bingham, and E. A. Williams, "Filamentation of Laser Light in Flowing Plasmas," *Phys. Fluids* **25**, 2302-2303 (1982).

B. Yaakobi, D. M. Villeneuve, M. C. Richardson, J. M. Soures, R. Hutchison, and S. Letzring, "X-Ray Spectroscopy Measurements of Laser-Compressed, Argon-Filled Shells," *Opt. Commun.* **43**, 343-346 (1982).

Forthcoming Publications

K. Lee, "Comments on 'Transverse Electromagnetic Waves with $\vec{E} \parallel \vec{B}$,'" accepted for publication by *Physical Review Letters*.

J. Reynolds, "Information Management Data Base for Fusion Target Fabrication Processes," accepted for publication by *Journal of Vacuum Science and Technology*.

T. F. Powers and J. R. Miller, "Rotational-Shearing Interferometric

Characterization of Inertial Fusion Targets," accepted for publication by *Journal of Vacuum Science and Technology*.

H. Kim, J. Mason, and J. R. Miller, "High-Z-Doped Laser Fusion Target Ablation Layers Using Metal Colloids and Metal-Substituted Sulfonated Polystyrene," accepted for publication by *Journal of Vacuum Science and Technology*.

B. A. Brinker, J. M. Cavese, J. R. Miller, S. G. Noyes, S. Sheble, and L. T. Whitaker, "Inertial Fusion Target Mounting Methods: New Fabrication Procedures Reduce the Mounting Support Perturbation," accepted for publication by *Journal of Vacuum Science and Technology*.

S. P. Sarraf, E. A. Williams, and L. M. Goldman, "Ion-Ion Two-Stream Instability in Multispecies Laser-Produced Plasma," accepted for publication by *Physical Review A: General Physics*.

Conference Presentations

S. Skupsky, R. L. McCrory, R. S. Craxton, J. Delettrez, R. Epstein, K. Lee, and C. P. Verdon, "Irradiation Uniformity for Laser-Driven Fusion," presented at the Sixth International Workshop on Laser Interaction and Related Plasma Phenomena, Monterey, California, October 1982.

B. Yaakobi, J. Delettrez, R. L. McCrory, R. Marjoribanks, M. C. Richardson, D. Shvarts, S. Skupsky, J. M. Soures, C. Verdon, D. M. Villeneuve, T. Boehly, R. Hutchison, and S. Letzring, "Thermal Transport Measurements in 1.05- μm Laser Irradiation of Spherical Targets," presented at the Sixth International Workshop on Laser Interaction and Related Plasma Phenomena, Monterey, California, October 1982.

L. Forsley, "Recursive Defining Words," presented at the 1982 Forth Laboratory Conference, Asilomar, California, October 1982.

R. L. Keck, "Forth in the Laboratory," presented at the 1982 Forth Laboratory Conference, Asilomar, California, October 1982.

J. D. Kafka, I. N. Duling III, T. Sizer II, C. W. Gabel, and G. A. Mourou, "Design and Operation of Synchronous Amplifiers for Subpicosecond Pulses," presented at the Optical Society of America Conference, Tucson, Arizona, October 1982.

J. H. Kelly, L. Iwan, and K. Walsh, "Preliminary Results in Stress-Induced Birefringence in the Nearly Athermal Glass LHG-8," presented at the Optical Society of America Conference, Tucson, Arizona, October 1982.

R. Bossert, S. Jacobs, and L. Lund, "Monolithic Cell for Frequency Conversion," presented at the Fourteenth Annual Symposium on Optical Materials for High-Power Lasers, Boulder, Colorado, November 1982.

J. A. Abate, R. Roides, S. D. Jacobs, W. Piskorowski, and T. Chipp, "Laser-Damage Thresholds of Optical Coatings at 351 nm," present-

ed at the Fourteenth Annual Symposium on Optical Materials for High-Power Lasers, Boulder, Colorado, November 1982.

The following presentations were made at the Twenty-Ninth National Symposium of the American Vacuum Society, Baltimore, Maryland, November 1982:

R. L. McCrory, "Target Requirements for Direct-Drive UV-Laser Fusion: Irradiation Uniformity and Hydrodynamic Stability."

D. Glocker, "Biased Ion Beam and Magnetron Sputtering of ICF Target Pusher Layers."

H. Kim, J. Mason, and J. Miller, "Homogeneous Metal Incorporation into Ablation Layer of Inertial Fusion Targets Using Sulfonated Polystyrene."

T. F. Powers and J. R. Miller, "Rotational-Shearing Interferometric Characterization of Inertial Fusion Targets."

J. R. Miller, "Inertial Fusion Target Mounting-Methods: New Fabrication Procedures Reduce the Mounting Support Perturbation."

H. Kim, T. Powers, and J. Mason, "Inertial Fusion Target Fabrication Using Polystyrene Mandrels."

J. P. Drumheller, "A Drill, Fill, and Plug Technique for Fabrication of Glass-Sealed Inertial Fusion Targets Containing Non-Permeable Gases."

J. Mason and H. Kim, "Metal Incorporation into Inertial Fusion Target Ablation Layers: 1. Polymer Stabilized Transition Metal Colloidal Dispersions."

J. Reynolds, "An Interactive Data Base for Fusion Target Fabrication Processes."

The following presentations were made at the Twenty-Fourth Annual Meeting of the APS Division of Plasma Physics, New Orleans, Louisiana, November 1982:

R. S. Marjoribanks, M. C. Richardson, and S. A. Letzring, "X-Ray Transmission-Grating Streak Spectrograph."

M. C. Richardson, B. Yaakobi, J. Delettrez, A. Entenberg, S. Kacendar, S. Letzring, R. Marjoribanks, D. M. Villeneuve, and J. M. Soures, "24-Beam Implosion of Large-Aspect-Ratio Ar-DT Targets."

J. Rizzo, S. Letzring, M. C. Richardson, and R. S. Craxton, "Spatial and Spectral Features of Harmonic Emission from Multibeam Irradiated Spherical Targets."

R. S. Marjoribanks, M. C. Richardson, S. A. Letzring, and J. Delettrez, "Time-Resolved X-Ray Spectroscopy (1-25 Å) of Symmetrically Driven Targets."

W. D. Friedman, S. A. Letzring, and M. C. Richardson, "Streaked X-Ray Backlighting Diagnostic for OMEGA."

- K. Tanaka, L. M. Goldman, W. Seka, and J. M. Soures, "Scattered Light Measurements around ω_0 from UV-Laser Plasmas."
- A. Simon, R. W. Short, E. A. Williams, and T. Dewandre, "Improved Evaluation of the Inhomogeneous $2\omega_p$ Instability Threshold."
- W. Seka, L. M. Goldman, J. M. Soures, K. Tanaka, and E. A. Williams, "Spectral Splitting of $3/2 \omega_0$ and $\omega_0/2$ Scattered Light from UV-Laser Plasmas."
- R. L. McCrory, C. P. Verdon, and J. Delettrez, "Numerical Simulations of Low-Intensity, 1.054- μm Glass Microballoon Implosions."
- B. Afeyan, E. Williams, R. Short, and A. Simon, "Oblique Incidence and Pump Polarization Effects on the $2\omega_p$ Instability in an Inhomogeneous Plasma."
- R. S. Craxton and R. L. McCrory, "Refractive Effects in Laser-Plasma Interaction Experiments."
- J. Delettrez, B. Yaakobi, M. C. Richardson, T. Boehly, R. S. Marjoribanks, S. Letzring, R. Hutchison, R. L. McCrory, and J. M. Soures, "Energy Transport and Partitioning in Nanosecond 1- μm Spherical Target Irradiation Experiments."
- R. L. Keck, L. M. Goldman, W. Seka, J. M. Soures, and E. A. Williams, "Continuum X-Ray Measurements of 1.06- and 0.35- μm Laser-Produced Plasmas."
- R. W. Short and E. A. Williams, "Spectral Broadening Arising from Filamentation in Laser-Plasma Interactions."
- B. Yaakobi, A. J. Burek, J. Boles, J. Hoose, O. Barnouin, R. Boni, L. M. Goldman, M. C. Richardson, W. Seka, and J. M. Soures, "Focusing X-Ray Crystal Devices for Target Implosion Diagnosis."
- J. Hoose, L. Iwan, J. Kelly, K. Lee, L. Lund, R. L. McCrory, M. C. Richardson, S. Skupsky, J. M. Soures, D. M. Villeneuve, and C. Verdon, "Progress in the Study of Uniformity Requirements for Direct-Drive Laser Fusion."
- S. Letzring, B. Yaakobi, J. Delettrez, R. Hutchison, R. Marjoribanks, R. L. McCrory, M. C. Richardson, J. M. Soures, and D. Villeneuve, "Transport Measurements on Symmetrically Irradiated Spherical Targets."
- M. C. Richardson, "Progress Toward Direct-Drive Laser Fusion."
- C. P. Verdon, R. L. McCrory, S. Skupsky, K. L. Lee, D. Villeneuve, and M. C. Richardson, "Two-Dimensional Numerical Simulations of Implosions Subject to Imposed Laser Nonuniformities."
- E. Williams, R. Short, and A. Simon, "Phase Integral Techniques in the Solution of Coupled-Wave Instability Problems in Inhomogeneous Plasmas."
- D. M. Villeneuve, W. Friedman, J. Hoose, S. Letzring, M. C. Richardson, K. Lee, S. Skupsky, and J. M. Soures, "Irradiation Uniformity of Spherical Targets on OMEGA."
- S. Skupsky and K. Lee, "Uniformity of Illumination for Laser-Driven Fusion."

The work described in this volume includes ongoing research at the Laboratory for Laser Energetics which is supported in part by Empire State Electric Energy Corporation (ESEERCO), General Electric Company, New York State Energy Research and Development Authority (NYSERDA), Northeast Utilities, The Standard Oil Co. (OHIO), University of Rochester, and various United States Government agencies, including Department of Energy, Air Force Office of Scientific Research, National Institutes of Health, and National Science Foundation.